Università degli Studi di Pavia

Facoltà di Ingegneria

Dipartimento di Ingegneria Civile e Architettura

TOWARDS AN ACCURATE SIMULATION OF COMPLEX CONTACT INTERACTIONS IN BIOMECHANICS PROBLEMS USING ISOGEOMETRIC 3D SOLID OR KIRCHHOFF-LOVE SHELL ELEMENTS.

Verso simulazioni accurate di complesse interazioni di contatto in campo biomeccanico, usando elementi isogeometrici 3D solidi o elementi shell Kirchhoff-Love.

Supervisor: Professor
ALESSANDRO REALI

Co - supervisors:
DOTT. MAURO FERRARO
DOTT. SIMONE MORGANTI

Author:
MARGHERITA CODA
UIN **414249**

Academic year 2014/2015

Ai miei genitori...
...ed alla mia cara nonna Giovanna

Acknowledgments

I want to thank Professor Alessandro Reali and Dott. Mauro Ferraro, for the confidence in me that they have always shown, for their great support and so much help. I will always be grateful to you for all you have done for me.
Thanks also to Dott. Simone Morganti for his assistance during this thesis work and to Professor R. L. Taylor, for helping me solving my issues with FEAP.
Thanks to my mum, my dad, Lorenzo and Beatrice and all the members of my family. Without your love and constant help, it would have been impossible to become who I am and to do what I did during all these years. In particular, a very big big hug to my super grandmum Giovanna: even if you are somewhere in Heaven, your lessons are still very precious to me.
Finally, thanks to all my friends: Selene, Federica and all the guys from "Lampedusa" office: Valentina, Rodrigo, Xi, Marco, Alice and Gianluca. You all made studying for the exams and working on my thesis work an exciting and joyful experience.

Abstract

This thesis work is aimed at investigating the potential benefits of a novel computational application, namely "Isogeometric Analysis", to reproduce the complex contact interactions typical of several biomechanical problems. In particular, the topic of computational contact is here discussed focusing on the formulation of "Normal Contact" as a constraint for non-penetration between the two contacting surfaces. These are described using a displacement-based formulation of both 3D solid and shell elements (based on Kirchoff-Love theory), with nodal displacements as variational variables, and discretized using NURBS, providing an exact description of the surfaces. For the numerical solution of these problems, the "Penalty Method" is used to fulfill the constraint equations in the normal direction in the contact interface. The main steps of the algorithm, computed by means of the Finite Element Analysis Program "FEAP", will be presented, together with several examples to compare Finite Element and Isogeometric Analysis and assess the effective and distinctive capabilities of the latter. As a future application, this algorithm may be applied to investigate the behaviour of many biological parts undergoing contact, e.g. to simulate the contact between leaflets of the aortic valve or to reproduce the interaction between a replacement valve wedged into the damaged aortic valve's place, in a minimally invasive surgical procedure known as "TAVI".

Sommario

Il presente lavoro di tesi mira ad investigare i potenziali benefici di un nuovo approccio computazionale, noto con il nome di “Analisi Isogeometrica”, per riprodurre le interazioni di contatto tipiche di molti problemi di biomeccanica. In particolare, l'argomento della modellazione computazionale del contatto viene qui discusso focalizzandosi sul contatto normale come vincolo di non penetrazione tra le superfici su cui il contatto si stabilisce. Tali superfici vengono descritte usando una formulazione agli spostamenti sia di elementi 3D solidi, che di elementi shell (basati sulla teoria di Kirchoff-Love), aventi come variabili variazionali gli spostamenti nodali. Inoltre, questi vengono discretizzati usando le “Non Uniform Rational B-Splines” (NURBS), capaci di fornire una descrizione esatta delle superfici. Relativamente alla soluzione numerica di questi problemi, una regolarizzazione di tipo “penalty” viene impiegata per soddisfare le equazioni di vincolo in direzione normale all'interfaccia su cui si stabilisce il contatto. Gli step principali dell'algoritmo, presente all'interno del software general purpose per l 'analisi agli elementi finiti FEAP, vengono presentati insieme con alcuni esempi volti a confrontare l'analisi agli elementi finiti con l'analisi isogeometrica, onde attestare le distintive e superiori capacitá di quest'ultima. Come applicazione futura, tale algoritmo puó essere applicato per investigare il comportamento di componenti biologiche sottoposte a contatto, ad esempio, per simulare il contatto tra i leaflet della valvola aortica o per roprodurre le interazioni tra una valvola sostitutiva artificiale posizionata in corrispondenza della sede della valvola aortica danneggiata, in una procedura minimamente invasiva nota con il nome di TAVI.

Contents

List of Tables

List of Figures

Chapter 1

Introduction

Cardiovascular Diseases (CVD) is a general term that is used to describe disorders that can affect the heart and/or blood vessels such as hypertension, coronary heart disease, heart failure or stroke. CVD are the leading cause of death in Western countries; a recent report of American Heart Association [39] states that an estimated 82.600.000 American adults (1 out of 3) have 1 or more types of CVD. Annually, CVD cause over 4 million deaths only in Europe, corresponding to the 42% of the overall mortality (as depicted in Figure 1.1). These numbers well explains the high incidence of such pathologies, which lead to high social and economical costs. As a matter of fact, CVD cause an estimated cost of €196 billions every year for the EU economy, in terms of direct cost and loss of productivity [30].
Valvular heart disorders represent a remarkable contribution to CVD. Nearly 30% of all adults over 65 have a sclerotic aortic valve (AV), 10% of which having accompanying stenosis [31]. More than 300.000 heart valve surgical operations were performed in 2006 worldwide [29].

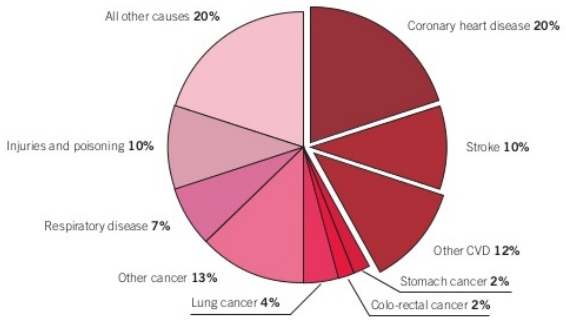

Figure 1.1: European CVD statistics: deaths divided by cause [30]

This observation is particularly meaningful if the influence of emerging technologies in both diagnosis and treatment of CVD is considered [2]; for example, modern techniques for generation and analysis of medical images allows accurate 3D reconstruction of several organs, the use of innovative materials to design miniaturized devices increases the number of interventional options adding new minimally-invasive procedures to classical open-heart surgery.
Design, development and performance assessment of the devices used in these procedures are the natural fields of application of computational biomechanics. The evolution of computational science has enabled the study of biomedical problems and structures, which are characterized by complex geometries, heterogeneous materials and whose functionality is determined by multiple concomitant factors. All these aspects may contribute to progressive advances in medicine enabling a change in its paradigm [2] Surgeon's experience is still the key factor for disease classification and treatment planning; the high inter-variability requires specific surgical procedures and prosthetic devices tailored to each specific patient, especially in pathologic situations where physiological and morphological alterations are severe. In this context, surgeon skills could be supported by predictive information and data derived by dedicated computational analyses. This concept can be referred to as "predictive biomedicine" [41] in which realistic computer-based simulations are performed both to evaluate the efficacy of different possible

treatments and to tailor surgical solutions based on patient-specific data, leading to a new paradigm in medicine which aims at reinforcing diagnosis with prediction. Obviously, in order to achieve such a challenging goal, a multidisciplinary approach, derived from a close collaboration between engineers and physicians, is necessary.
In this chapter the previous considerations are expanded through the biomechanical analysis of the AV, that is one of the two semilunar valves of the heart, the other being the pulmonary valve. It is comprised of an aortic root and three semilunar cusps or leaflets (Figure 1.2). Moreover, an overview of the biological prostheses used for the replacement of native AV either through open-surgery or percutaneous procedures is provided together with a review of the main computational methods used in biomechanics. In particular, the use of patient-specific finite element analysis (FEA) to assess the structural performance of (1) stentless biological prosthesis used for aortic valve replacement (AVR) and (2) transcatheter aortic valve implant (TAVI) is presented.

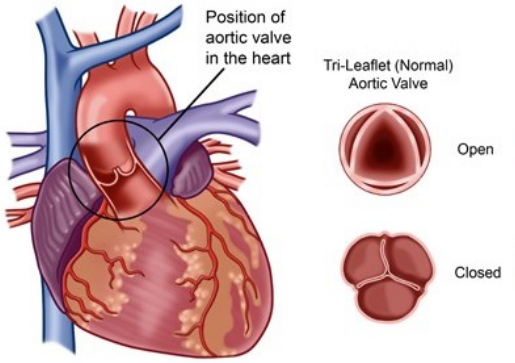

Figure 1.2: Native Aortic Valve

1.1 Open Heart vs. Minimally Invasive Surgery

Given the wide range of available treatment options, the classification of aortic valve surgery procedures is not trivial. In the following, such options are split with respect to the related interventional strategy, i.e., traditional open heart surgery or minimally-invasive.
In case of open heart surgery, prosthetic heart valves are mentioned. Prosthetic heart valves are valve substitutes that should mimic the characteristics of a normal native valve. In particular, it should have excellent hemodynamics, long durability, high thromboresistance, and excellent implantability. Unfortunately, this ideal valve substitute does not exist, and each of the currently available prosthetic valves has inherent limitations [34]. They exist in three basic types: bileaflet, monoleaflet, and caged ball valves, according to the relative pathology (see Figure 1.3). For an overview of the current state of knowledge and future perspectives with regard to optimal prosthesis selection and clinical management after valve implantation, reference is made to [34].

1.1.1 Open Heart Surgery

Different surgical treatments are nowadays adopted to restore valve functionality. In literature many techniques for aortic root reconstruction are described, either sparing the valve leaflets [13, 40] or involving the use of mechanical, stented [32, 42], or stentless biological prostheses [38] as well as homograft and allograft valves [15, 46] that can be either stented or stentless.
On the one hand, mechanical prostheses assure a long-term solution due to an excellent durability [23], on the other hand, they are associated with a greater incidence of hemorrhage than bioprostheses since they do not avoid the use of anticoagulants. Moreover, bioprostheses are associated with more physiological hemodynamics as well as a minor trombogeneticity [33]; accordingly, biological valves assure greater performances than mechanical ones and, in particular, stentless valves are preferable

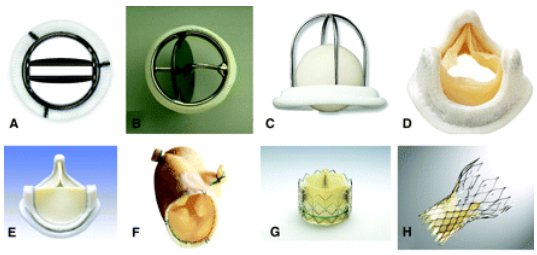

Figure 1.3: Different types of prosthetic valves. A, Bileaflet mechanical valve (St Jude); B, monoleaflet mechanical valve (Medtronic Hall); C, caged ball valve (Starr-Edwards); D, stented porcine bioprosthesis (Medtronic Mosaic); E, stented pericardial bioprosthesis (Carpentier-Edwards Magna); F, stentless porcine bioprosthesis (Medtronic Freestyle); G, percutaneous bioprosthesis expanded over a balloon (Edwards Sapien); H, self-expandable percutaneous bioprosthesis (CoreValve)

than stented ones, representing an excellent option for aortic valve replacement. The use of stentless valves, in fact, appears to potentially increase the long-term survival when compared to stented ones due to improved ventricular reverse remodeling [3]. At the same time, the hemodynamics is closer to physiologic behavior; additionally, the use of a continuous suture technique reduces the crossclamp times and cardiopulmonary bypass. However, open heart surgery with cardiopulmonary bypass is not always recommended: in presence of coexisting conditions such as advanced age, congestive heart failure, coronary artery disease, lung disease and renal insufficiency, the surgical risk becomes very high and, in some cases, unsustainable [9].

1.1.2 Minimally Invasive Surgery of Aortic Stenosis

Aortic stenosis is described as an obstruction of flow at the level of the AV (Figure1.4). In particular, there are mainly three causes of stenosis: (i) calcifications related to atherosclerosis, which can be roughly defined as an inflammatory disease impairing valve patency; (ii) endocarditis, i.e., an infection caused by the presence of bacteria in the bloodstream and bacterial vegetations on valve leaflets; (iii) congenital diseases and, in particular, bicuspid aortic valve, which consists in the fusion of two leaflets [2].

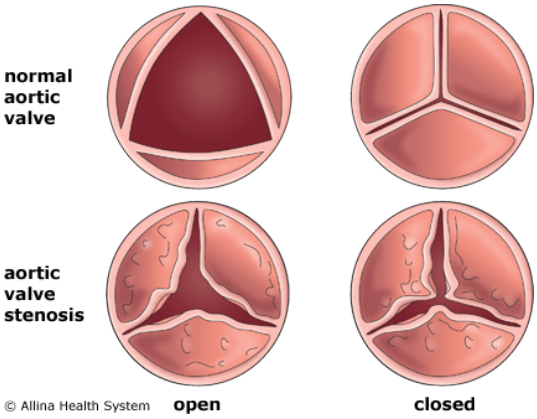

Figure 1.4: Stenotic Aortic Valve

New developments in cardiothoracic surgery led to innovative minimally invasive devices for the treatment of aortic stenosis in patients associated with potential high surgical risk [2]. In the last decade, several devices were designed and submitted to clinical evaluation [8, 19] confirming that, on one hand, such innovative techniques represents a promising solution for aortic stenosis even though, on the other hand, at present, it is still an immature procedure due to limited follow-up data and durability evaluation.

Different transcatheter devices are currently available and they consist of either a stainless steel balloon-expandable (Edwards Sapien) or nitinol self-expandable stent (Medtronic CoreValve). Baloon-expandable devices can also be made of cobalt chromium. In fact, the very last prosthetic devices belonging to this ategory are named SAPIEN XT and are made of an innovative cobalt chromium alloy (see Fig. 1.5).

Figure 1.5: Transcatheter aortic valve prostheses currently used in clinical practice: the Medtronic CoreValve (left) and the Edwards SAPIEN XT (right)[2]

In both cases, a tri-foliate bovine/porcine pericardium heart valve is attached inside the cylindrical metallic frame. Prosthesis placement can be achieved by either a trans-femoral or trans-apical access. In the first case, the prosthetic device is inserted through the femoral artery and passes retrogradely through the aorta until the aortic root is reached [43] while, in the second case, it is placed directly through the apex of the heart [27]. Once the valve has been positioned, in case of balloon-expandable devices, a balloon inflation leads to the valved stent expansion which excludes and compresses the native diseased leaflets. Self-expandable valve placement procedure is very similar to the previously-mentioned procedure except that self-expandable prostheses automatically open through a step-wise deployment when gradually extracted from the delivery catheter. Particular attention must be devoted to positioning, which is crucial since it affects post-operative performance: on one hand, the implanted valve must guarantee regular flow through the coronaries while, on the other hand, the prosthesis should not overlap and crush the left bundle branch [35] to avoid is a cardiac conduction abnormality.

1.2 Biomechanics by means of computational tools

In both cases the mechanical and functional performance of the implanted devices is difficult to be evaluated. Therefore, the structural computational framework commonly known as Finite Element Analysis (FEA) is used to investigate either aortic valve biomechanics in both healthy and diseased conditions or to design and evaluate prosthetic devices. In particular, FEA of the aortic valve can be applied to:

- *Geometrical modeling* of the human trileaflet AV [25];
- Study of the *pathologies* of the AV ([18, 17]);
- *Dynamical behavior* of the AV throughout the cardiac cycle ([6, 16]):
- *Prediction of the outcomes* of AV surgery [17].

In the next paragraph the role and main features of computational tools is specialized focusing on the aortic valve. Moreover, a brief overview of FEA theory is provided.

1.2.1 The role of computational tools in clinical and industrial problems

As already mentioned, modern computational methods are an ubiquitous tool to reproduce various clinical procedures for pre-operative planning and to predict the mechanical behavior of a wide range of medical devices. The major benefit of the employment of computational methods for the mechanical evaluation of medical devices is the possibility to test different combinations of materials, geometries and working conditions prior to prototype manufacturing or when the traditional experimental approach is too expensive or difficult to implement [14]. Moreover, computational methods are the key ingredient of the concept of "predictive medicine" [41], i.e., the family of methods and techniques whose main goal is predicting the outcomes of alternative treatment plans for an individual patient.
A computational method should be able to describe precisely the geometry of the object under study, tipically identified by a parametric Computer Aided Design (CAD) model, and to perform accurate simulations in short time. Such characteristics are fundamental to obtain reliable results. Starting from medical images, three-dimensional models of the object of interest are obtained by means of computational tools. In literature, several techniques exist to get these 3D representations. For example, the main steps that are required for the creation of a patient specific aortic root model according to [2] are summarized in Figure (1.6). Once having the CAD models, different analysis can be performed.

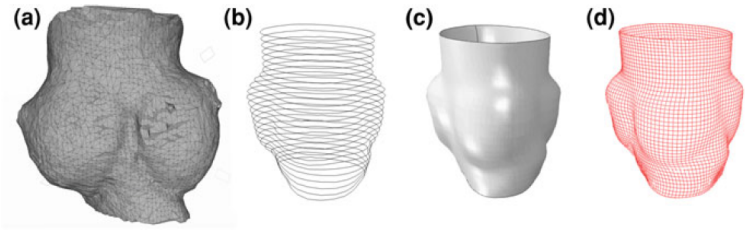

Figure 1.6: Creation of aortic root model: **a** an STL file is extracted from medical images by appropriate processing; **b** a series of splines identifying the aortic root wall are obtained elaborating the STL file; **c** a CAD model of the aortic root is obtained through lofting; d a structured mesh is derived from the CAD model

Moreover, in order to be reliable in real life clinical and industrial problems, they calls for a deep comprehension of the different sources of complexity related to the problem itself [14], which are:

- *Geometry description*: it is one of the most important factor to be taken into account. The more precise is the real geometry, the more accurate are the results. For example, focusing on the AV and, in particular, taking into account a stentless prosthesis model, the prosthetic leaflet geometry plays a key-role for efficacy and durability in AVR procedures. For this reason, it must be precisely reproduced in order to predict the realistic valve behavior [45]. Several geometrical guidelines exist to create the model of the valve. Among them, Labrosse's geometrical guidelines [25] are those described in [2]. They call for the model to be completely described by five parameters [1].

- *Material behavior*: it can be inherently linear or non linear, isotropic or anisotropic, etc. These characteristics are important because, according to them, the proper constitutive model is chosen to reproduce the major phenomena involved with the material behavior. As an example, the stentless valve is made of two bovine pericardial sheets without any fabric reinforcement and it is regarded as an isotropic material [26]. Consequently, an incompressible isotropic hyperelastic Mooney-Rivlin model can be adopted for the stentless valve leaflets [11].

- *Working conditions*: the device or anatomical part working conditions are to be reliably transposed into the computational model for each evaluation of a particular feature. For example, according to [2], in the case of the stentless prosthesis model of the AV, the prosthesis implant is simulated by constraining the attachment lines of prosthesis leaflets to overlap the so-called "suture-lines" that are defined on the patient specific aortic root model through a three steps pro-

cedure that is repeated for each one of the three aortic valve sinus and it is briefly summarized in Figure (1.7).

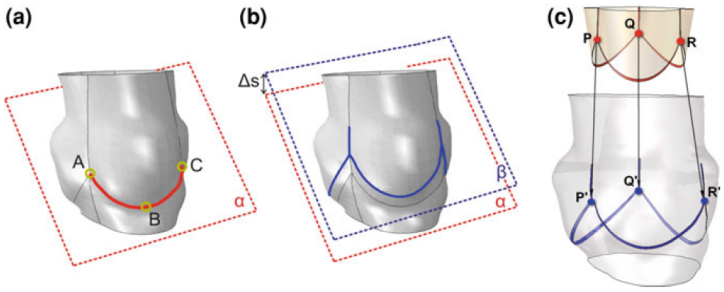

Figure 1.7: Definition of the suture lines: **a** the plane α containing the native line of attachment and passing through the points A, B and C is created; **b** the plane β is obtained translating a vertically; the line of attachment of the prosthesis leaflet is defined by the intersection of a with the sinus. The *blue lines* represent the whole set of attachment lines where the nodes of the prosthesis are tied with the nodes of the sinuses; **c** simulation strategy for the prosthesis placement: the black arrows represent the displacements to be computed and applied to the nodes of the prosthesis line of attachment

1.2.2 Finite Element Analysis

Finite element analysis is a computer-based method which had its origins in the early 1960s. It is nowadays the predominating method in structural analysis. Structures of arbitrary shapes for which no analytical solutions had existed before, can be analyzed and therefore designed with the introduction of the finite element method.
FEA decomposes the structural domain into many small, "finite" elements with simple shapes. These elements are defined by a set of nodal points, which are connected by basis functions. Linear polynomials are the most used basis functions, due to their semplicity. Afterward, an analysis-suitable geometry, i.e., a finite element mesh, is created. Although mesh generation to a large extent is performed automatically, it still requires manual control and adjustments by the engineer. In order to obtain reliable results, a series of analyses with different mesh refinements has to be performed. Every FE mesh is only an approximation to the original geometry and each finer mesh (i.e., a “refined” mesh) has to be completely rebuilt from the CAD geometry. The creation of an analysis-suitable geometry from the CAD geometry is nowadays the bottleneck for large engineering computations, and mesh creation is one part of this model transfer.

FEA can be used to perform prosthesis placement by imposing precomputed displacements to the nodes of the prosthesis attachment line (see Figure 1.7c). The result is the tensional state of each leaflet in terms of Von Mises stress (see Figure 1.8). FEA can be also used to better understand the mechanics and hemodynamics of TAVI device. TAVI is the short for “transcatheter aortic valve implant”. This clinical procedure is based on the use of one of the currently available percutaneous aortic valve prosthesis, i.e., the balloon expandable Edwards Lifescience Sapien valve which is basically composed of three flexible biological leaflets sutured on a stainless steel balloon-expandable stent [2]. Sapien placement can be achieved by either a trans-femoral or trans-apical access. In the first case, the prosthetic device is inserted through the femoral artery and passes retrogradely through the aorta until the aortic root is reached [43] while, in the second case, it is placed directly through the apex of the heart [27]. Once the device has been positioned, balloon inflation leads to the valved stent expansion which excludes and compresses the native diseased leaflets (Figure 1.9).
The simulation of TAVI with FEA allows to evaluate the impact of the prosthesis on the aortic root and the related Von Mises stress distribution along the vessel wall as depicted in Figure 1.10.

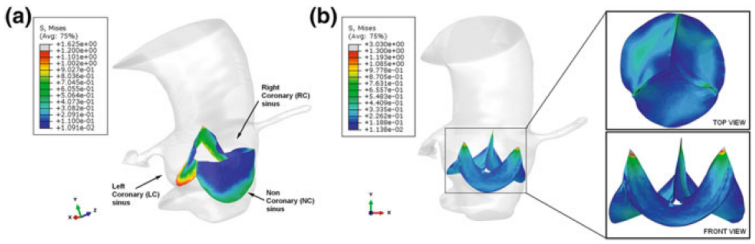

Figure 1.8: Simulation results: **a** the Von Mises stress contour plot, outcome of the simulation of prosthesis implant on a given the suture line is represented. Non Coronary (NC), Left Coronary (LC) and Right Coronary (RC) sinuses; **b** prosthesis placed on a given suture-line at the end of diastole: due to the asymmetry of the patient-specific sinuses, the non coronary leaflet of the virtually implanted symmetric valve closes below the other two leaflets. A central gap is highlighted from the front view which signifies that the replacement solution fails

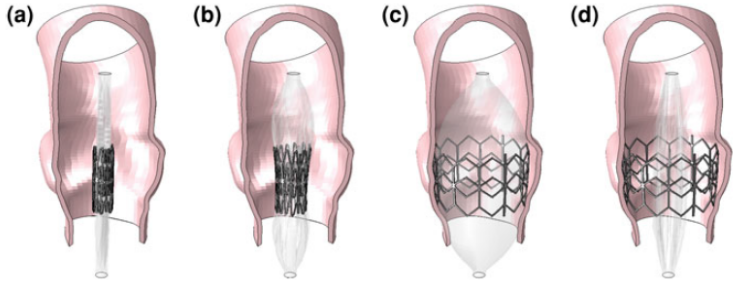

Figure 1.9: Different frames of balloon expansion and stent apposition (TAVI): **a** initial configuration; **b** the balloon starts to deploy the stent; **c** the balloon is fully expanded and the stent is fully deployed; **d** final configuration after balloon deflation [2]

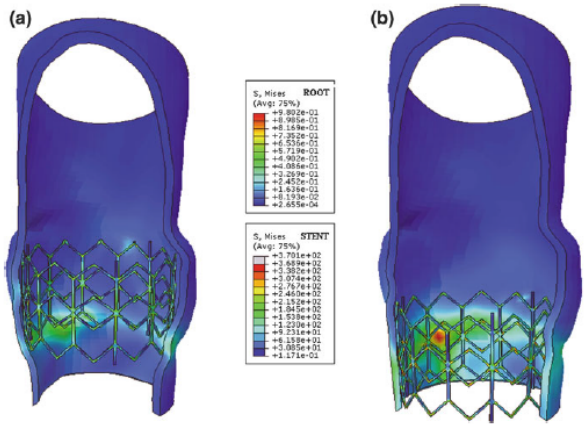

Figure 1.10: Simulation results (TAVI): the Von Mises stresses on the aortic root wall and stent struts are represented: **a** after the distal positioning; **b** after the proximal positioning [2]

A different positioning procedure (distal or proximal positioning) leads to different tensional state on the vessel wall which means different potential injury induced by the stent on the aortic root tissue.

Even if FEA is already a widely employed and well assessed simulation tool, it presents some limitations that can affect both the geometrical accuracy of the domain under investigation and the accuracy of

the approximated solution. In particular, low-order and low-regularity polynomials used to discretize the continuum domain do not allow, in general, to accurately represent complex geometries unless extremely fine meshes are adopted. The construction of the finite element mesh is costly and time consuming and it is the geometric approximation inherent in the mesh that leads to accuracy problems. At the same time, FEA basis functions do not allow a proper approximation of the solution without resorting to a high number of degrees of freedom, in particular when different sources of non linearity are present. Hence, non linear phenomena may not be fully understood and rendered by FEA. For example, one of the most intriguing and difficult non linear phenomenon is the contact between objects (e.g., the contact between leaflets of the AV). Contact description and detection requires the definition of some key geometrical quantities that sometimes are difficult to be properly individualized on the FE discretized model. This amply influence numerical results. To overcome some of the previous issues, Isogeometric Analysis (IgA), has been recently proposed as an exact geometry, cost-effective alternative to classical FEA [20], proposing to replace the low-order, low-regularity FEA basis functions with the high order, high-regularity basis functions employed in CAD while retaining an isoparametric framework. In particular, IgA has many features in common with FEA but it is more geometrically based and takes inspiration from CAD [20]. A primary goal is to be geometrically exact. Another goal is to simplify mesh refinement by eliminating the need for communication with the CAD geometry once the initial mesh is constructed. Yet another goal is to more tightly knot the mesh generation process within CAD. Given these statements, IgA seems indeed an ideal framework to address the FEA limitations highlighted above [14].
IgA is the computational method adopted in this thesis work. For the sake of clarity the most important differences between FEA and IgA are listed in Table 1.1.

FEA	IGA
Meshing process **necessary**, **costly** and **time consuming**	**No** meshing process required
Geometric representation **not** exact	**Exact** geometric representation
Refinement needs **new** meshing process	Efficient refinement **preserving geometry**
Low-order, **low** continuity elements can have problems in dealing with model non linearities, e.g., contact	**High**-order, **high** continuity elements can improve the reproduction of non linear phenomena

Table 1.1: Main differences between FEA and IgA

1.3 Aim of the thesis work

The previous sections describe how computational tools can potentially help clinical practice to reproduce many clinical procedures for pre-operative planning and to predict the mechanical behavior of a wide range of medical devices. The development of such tools requires deep knowledge of the object under study in terms of anatomy and behavior in different conditions, pathological or not. The most important requirement of computational tools is being able of reproducing real life experiments in terms of geometric description of the domain, but also in terms of regularity of the numerical solution. In this dissertation, the computational framework is explained from the well-known and widely employed FEA point of view as well as from Isogeometric Analysis outlook, a novel and cost-effective numerical technique. The basic idea is to develop a computational framework in which the traditional FEA basis functions were substituted with that one employed in CAD systems. This implies the ability to describe exactly the computational domain geometry throughout the analysis process, including, at the same time, the chance to adjust the basis functions continuity.
In this work, the focus is on the numerical study of the highly non linear phenomenon of the contact between bodies. More precisely, the NURBS-based isogeometric frictionless contact between bodies is presented, both from a theoretical and algorithmic point of view. This means that an isogeometric approach with NURBS as smooth parametric geometry is employed for the study of contact phenomena

where only normal forces are transmitted and therefore taken into account. The contact constraint is regularized with a penalty method. The domain of the bodies undergoing contact are discretized by using different kind of elements: three-dimensional and shell elements. Shell elements are tipically used to model structural behavior of curved bodies which have one dimension small (a thickness normal to the remaining surface coordinates) compared to the other dimensions of the surface.
With respect to the elements used to discretize the domain, contact investigation is accomplished in the following way:

- 3D Elements: contact study with practical examples;
- Shell Elements: preliminary investigation.

Several examples are provided in order to attest the superior ability of IgA to characterize and investigate non linear phenomena.

1.4 Organization of the dissertation

The thesis work is organized as follows:

- Chapter 2: Isogeometric analysis basic concepts

  In this chapter the basic concepts of B-splines and NURBS are described. Consequently, the basic IgA concepts are introduced with a focus on applications and comparison with traditional FEA.

- Chapter 3: Structural Mechanics of shells

  Shell elements are generally used to model structural behavior of curved bodies. Tipically, such curved bodies have one dimension smaller than the other dimensions of the surface. The smaller dimension is the thickness normal to the remaining surface coordinates. In this chapter, the fundamentals of continuum mechanics are reviewed by assuming large displacements and small strains from a Lagrangian point of view. Afterward, Kirchoff-Love shell theory is introduced.

- Chapter 4: IgA based contact mechanics

  One of the main advantages of IgA is the ability to provide a smooth basis capable of describing exactly the computational domain geometry throughout the analysis process, controlling at the same time function continuity. These IgA peculiar characteristics have been successfully applied on many critical aspect of FEA, including the highly non linear contact mechanics. This chapter focuses on the application of NURBS-based IgA to 3D frictionless contact problems between bodies.

- Chapter 5: Numerical Results

  The different capabilities of IgA and FEA to deal with non linear contact phenomena are tested by using the IgA contact driver presented in Chapter 4. Three different problems, characterized by increasing complexity are taken into account. The main steps that have been applied to perform the analysis are described in this chapter. Moreover, in order to estimate the suitability of the given approach, the convergence of IgA and FEA is evaluated by considering stored energy as a global reference quantity for the assessment with respect to the number of DOF.

- Chapter 6: Conclusions

  In this last chapter, the conclusions are drawn highlighting the original aspects of the thesis work. Moreover, further possible developments are illustrated.

Chapter 2

Isogeometric Analysis Fundamentals

In this chapter, the basic concepts of Isogeometric Analysis are introduced (for a full comprehension of the latter, please refer to [7], [36]). The discussion firstly focuses on curves representation and then it will be extended to surfaces and trivariate solids. The continuum discretization employed within the IgA framework adopted in this thesis work, is entirely based on such NURBS structures. Since NURBS are built from B-Splines and B-Splines have emanated from Bézier curves, the "real" first antecedents of NURBS were Bézier curves. Hence, this section starts with a short review of Bézier curves as an introduction to B-Splines. B-Spline curves, surfaces and trivariate solids are explained in more detail since most of the definitions and properties of B-Splines apply to NURBS as well. Finally, NURBS as a generalization of B-Splines are presented.

2.1 Bézier Curves

A fitting curve is a curve that should approximate a set of given points. Data points are represented exactly if an interpolating polynomial is used. However, oscillations between the points can occur, see Figure (2.1)(a). A Bézier curve is an approximating curve, where data points, called "control points", are not interpolated but only approximated. Therefore, a smooth and non-oscillating curve is obtained and the curve "stays inside" the control polygon, see Figure (2.1)(b). The control polygon is the linear connection of the control points: only the first and the last point of the control polygon are interpolated.

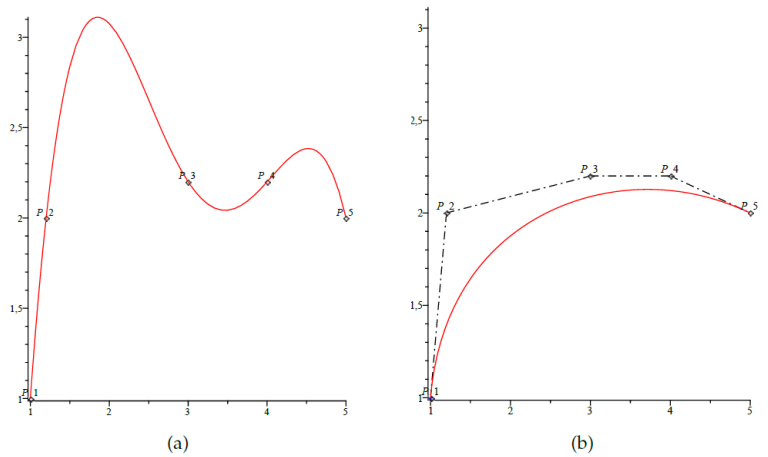

Figure 2.1: Fitting data points. (a) Interpolating polynomial. (b) Approximating Bézier curve

A Bézier curve is defined by the linear combination of basis functions and control points:

$$C(\xi) = \sum_{i=1}^{n} B_{i,p}(\xi) P_i \tag{2.1}$$

where n is the number of control points and $B_{i,p}(\xi)$ are the Bernstein polynomials of polynomial degree p. The polynomial degree is related to the number of control points by: $p = n\text{-}1$. The Bernstein polynomials are defined by:

$$B_{i,p}(\xi) = \frac{n!}{i!(n-i)!} \xi^i (1-\xi)^{n-i}. \tag{2.2}$$

In this form, ξ is defined as $\xi \in [0, 1]$. The problem of Bézier curve is that with an increasing number of control points, the polynomial degree has to be increased. Furthermore, with increasing polynomial degree the approximation to the control polygons deteriorates and so the algorithms get numerically instable. In addition, the global support of the basis functions is a problem itself for geometric modeling, because it means that any modifications of a control point has influence on the whole curve and no local changes can be made to the curve. Finally, no points of reduced continuity (e.g. kinks) can be inserted inside the curve. These problems can be solved by using B-Splines.

2.2 B-Splines

B-Spline curves, similar to Bézier curves, are defined by a linear combination of control points and basis functions over a parametric space. The basis functions are called B-Splines (short for "Basis Splines"). The parametric space is divided into intervals and the B-Splines are defined piecewise on these intervals, with certain continuity requirements between them. The number of intervals is arbitrary and so the polynomial degree can be chosen independently of the number of control points. Consequently, a large number of data points can be approximated using a low polynomial degree. This is illustrated in Figure (2.2). Seven control points are approximated once by a Bézier curve with $p{=}6$ (a) and once by a B-Spline curve with $p{=}3$ (b).

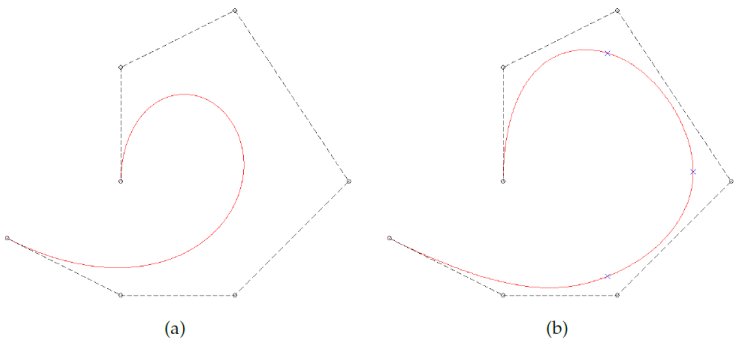

Figure 2.2: Fitting data points. (a) Bézier curve, p = 6. (b) B-Spline curve, p = 3.

The B-Spline curve in Figure (2.2)(b) consists of four sections, as a consequence of the lower polynomial degree. The limits of these sections are called knots and are indicated by small crosses on the curve. As can be seen, the B-Spline curve stays closer to the control polygon due to the lower polynomial degree. B-Spline basis functions are defined to be unequal to zero only on a restricted range of intervals which means a local influence of the control points on the curve. Furthermore, it is possible to reduce the continuity in the basis functions between intervals and therefore create kinks inside a curve.

2.2.1 Knot Vector

A knot vector in one dimension is a set of coordinates in the parametric space in non-descending order, written $\Xi = [\xi_1, \xi_2, ..., \xi_{n+p+1}]$, where $\xi_i \in \mathbb{R}$ is the ith knot, i is the knot index, $i = 1,2,...,n + p + 1$, p is the polynomial order and n is the number of basis functions (and control points) which

comprise the B-Spline. It divides the parametric space into sections. If all knots are equally-spaced in the parametric space, they are said to be *uniform*. If they are unequally spaced, they are *non-uniform*. More than one knot can be located at the same coordinate in the parametric space. These are referred to as *repeated* knots. A knot vector is said to be *open*, *clamped*, or *nonperiodic* if its first and last knots appear exactly $p + 1$ times. In this work the term "open" is used. A B-Splines basis function is C^{∞} continuous inside a knot span, i.e. between two distinct knots, and C^{p-1} continuous at a single knot. At a knot of multiplicity k, the continuity is C^{p-k}, i.e. by increasing the multiplicity of a knot, the continuity can be decreased. In case of a B-Spline with an open knot vector, the first and the last control points are interpolated: accordingly, the curve is tangential to the control polygon at the start and at the end of the curve. Open knot vectors are standard in the CAD literature.

2.2.2 Basis Functions

Given a knot vector and the polynomial degree, B-splines basis functions can be computed by the *Cox-deBoor* recursion formula. It starts with p=0, i.e. with piecewise constants:

$$N_{i,0}(\xi) = \begin{cases} 1 & \xi_i \leq \xi \leq \xi_{i+1} \\ 0 & otherwise \end{cases} \tag{2.3}$$

For $p \geq 1$ it is,

$$N_{i,p}(\xi) = \frac{\xi - \xi_i}{\xi_{i+p} - \xi_i} N_{i,p-1}(\xi) + \frac{\xi_{i+p+1} - \xi}{\xi_{i+p+1} - \xi_{i+1}} N_{i+1,p-1}(\xi). \tag{2.4}$$

Important properties of B-Splines basis functions are:

- They constitute a partition of unity, that is, $\forall \xi$

$$\sum_{i=1}^{n} N_{i,p}(\xi) = 1; \tag{2.5}$$

- Local support, i.e. a basis function $N_{i,p}$ is non-zero only in the interval $[\xi_i, \xi_{i+p+1}]$;
- Non negativity, i.e. $N_{i,p}(\xi) \geq 0$;
- Linear independence, i.e. $\sum_{i=1}^{n} \alpha_i N_{i,p}(\xi) = 0 \Leftrightarrow \alpha_j = 0, j = 1, 2, ..., n.$

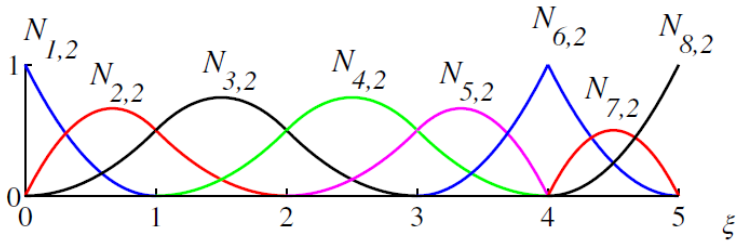

Figure 2.3: Quadratic basis functions for open, non-uniform knot vector $\Xi = [0, 0, 0, 1, 2, 3, 4, 4, 5, 5, 5]$. [7].

Figure (2.3) shows an example of quadratic basis functions for the open, non uniform knot vector

$$\Xi = [\xi_1, \xi_2, \xi_3, \xi_4, \xi_5, \xi_6, \xi_7, \xi_8, \xi_9, \xi_{10}, \xi_{11}] = [0, 0, 0, 1, 2, 3, 4, 4, 5, 5, 5].$$

Many things must be noted given this knot vector: the basis functions are interpolatory at the ends of the interval and also at $\xi = 4$, which corresponds to a location of a repeated knots. At this repeated

knot, only C^0-continuity is attained. Elsewhere, the functions are C^1-continuous.
To fully understand how the continuity across an interior element boundary is a direct result of the polynomial order and the multiplicity of the corresponding knot value, Figure (2.4) must also be discussed. It shows a fourth order curve with different level of continuity at every element boundary:

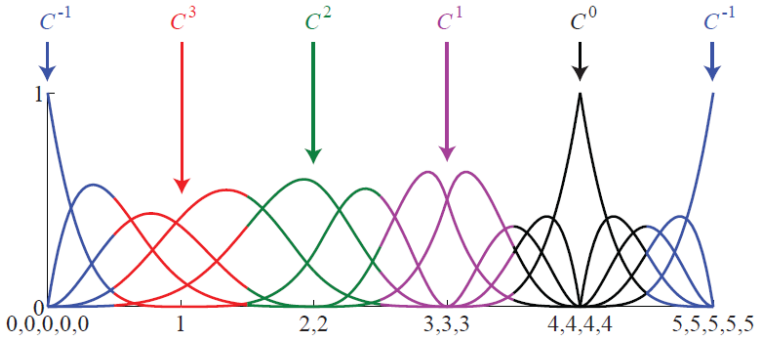

Figure 2.4: Quartic (p = 4) basis functions for the open, non-uniform knot vector $\Xi = [0, 0, 0, 1, 2, 3, 4, 4, 5, 5, 5]$ [7].

- At the first internal element boundary, $\xi = 1$, the knot value appears only once in the knot vector. Thus, the maximum level of continuity possible ($C^{p-1} = C^3$, with $p = 4$) is achieved.
- At each subsequent internal knot value, the multiplicity is increased by one, and so the number of continuous derivatives is decreased by one.
- At $\xi = 4$ the knot value is repeated exactly p times. The C^0 basis function is therefore interpolatory. In such case, all basis functions at this knot vanish, except one, which takes on the value 1.
- The basis is also interpolatory at the boundary of the domain, where the open knot vector demands that the first and last knot value be repeated $p+1$ times. In this case, the results is "C^{-1}" continuous, i.e. the basis is fully discontinuous, naturally terminating the domain.
- Increasing the multiplicities of the knots *seems* to have decreased the support of some of the functions. This does not contradict what stated before about local support of the basis functions: actually, the support of each function $N_{i,p}$ still begins at knot ξ_i and ends at ξ_{i+p+1}, which means that the support of each function is still $p+1$ knot spans, but some of those knot spans have zero measure due to the repetition of knot values. For the sake of clarity, the same concept is illustrated in Figure (2.5), where a B-Spline curve is modified by changing the y-coordinate of the last control points. This modification affects the curve *only* in the last sections, whereas if one of the inner control points is modified, it has influence on a couple of sections, at maximum on p+1 sections.

The first derivatives of B-Spline basis functions are represented in terms of B-Splines low order bases. For a given polynomial order and knot vector Ξ, the derivative of the i^{th} basis function is given by:

$$\frac{d}{d\xi}N_{i,p}(\xi) = \frac{p}{\xi_{i+p} - \xi_i}N_{i,p-1}(\xi) - \frac{p}{\xi_{i+p+1} - \xi_{i+1}}N_{i+1,p-1}(\xi). \tag{2.6}$$

Equation (2.6) can be generalized to higher order derivatives, by differentiating both sides. It results in equation (2.7):

$$\frac{d^k}{d^k\xi}N_{i,p}(\xi) = \frac{p}{\xi_{i+p} - \xi_i}\left(\frac{d^{k-1}}{d^{k-1}\xi}N_{i,p-1}(\xi)\right) - \frac{p}{\xi_{i+p+1} - \xi_{i+1}}\left(\frac{d^{k-1}}{d^{k-1}\xi}N_{i+1,p-1}(\xi)\right). \tag{2.7}$$

Expanding (2.6) by means of (2.7), the following formula, purely expressed in terms of lower order functions $N_{i,p-k}, ..., N_{i+k,p-k}$, can be obtained:

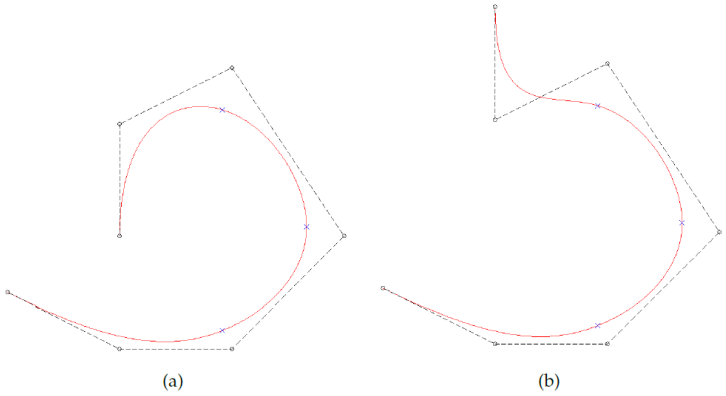

Figure 2.5: Local influence of control points on B-Spline curves. (a) Initial curve. (b) The same curve with the last control point modified.

$$\frac{d^k}{d^k\xi}N_{i,p}(\xi) = \frac{p!}{(p-k)!}\sum_{j=0}^{k}\alpha_{k,j}N_{i+j,p-k}(\xi), \tag{2.8}$$

with

$$\begin{aligned}
\alpha_{0,0} &= 1, \\
\alpha_{k,0} &= \frac{\alpha_{k-1,0}}{\xi_{i+p-k+1}-\xi_i}, \\
\alpha_{k,j} &= \frac{\alpha_{k-1,j}-\alpha_{k-1,j-1}}{\xi_{i+p+j-k+1}-\xi_{i+j}} j = 1, ..., k-1, \\
\alpha_{k,k} &= \frac{-\alpha_{k-1,k-1}}{\xi_{i+p+1}-\xi_{i+k}}.
\end{aligned}$$

The denominator of several of these coefficients can be zero in the presence of repeated knots. Whenever this happens, the coefficient is defined to be zero. If an open knot vector is used, the following effects on basis functions and their derivatives can be observed:

- At $\xi = 0$ all basis function except the first one vanish:

$$\begin{aligned}
N_{1,p}(0) &= 1, \\
N_{1,p}(0) &= 0, \quad i \neq 1
\end{aligned} \tag{2.9}$$

- With regard to the first derivatives, only the first two are non zero. In particular:

$$\begin{aligned}
N'_{1,p}(0) &= -\tfrac{p}{\xi_{p+2}}, \\
N'_{2,p}(0) &= \tfrac{p}{\xi_{p+2}}, \\
N'_{i,p}(0) &= 0, \quad i > 2
\end{aligned} \tag{2.10}$$

  Thus, $N'_{1,p}(0) = -N'_{2,p}(0)$ holds.

- The same applies to the basis functions at the end of the parametric space.

Previous results can be seen in Figure(2.6).

2.2.3 B-Splines Curves

Similar to Bézier curve, a B-Spline curve of degree p is given by the linear combination of control points and the respective basis functions:

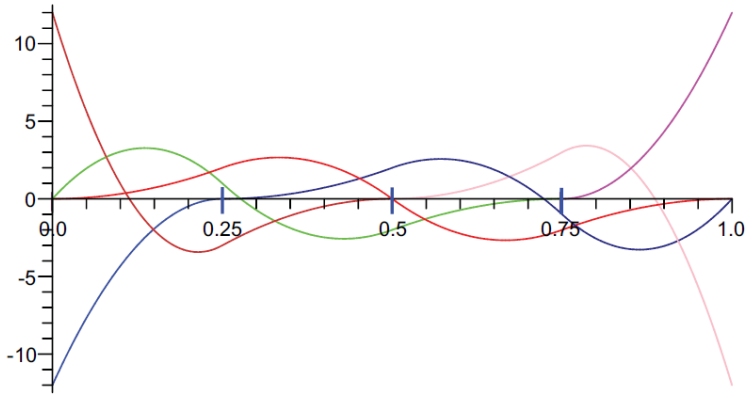

Figure 2.6: First derivatives of cubic B-Spline basis functions with open knot vector $\Xi = [0, 0, 0, 0, 0.25, 0.5, 0.75, 1, 1, 1, 1]$ [22].

$$C(\xi) = \sum_{i=1}^{n} N_{i,p}(\xi) P_i. \tag{2.11}$$

The first derivative of the curve is computed by the linear combination of control points and the first derivative of the respective basis functions:

$$C'(\xi) = \sum_{i=1}^{n} N'_{i,p}(\xi) P_i. \tag{2.12}$$

In Figure (2.2)(b), a cubic B-Spline with an open knot vector is given. The first and last control points are interpolated and the curve is tangential to the control polygon at its start and end. This is a direct consequence of using an open knot vector. It can be understood by inserting Equations (2.9) and (2.10) into (2.11) and (2.12). These results are obtained:

$$C(0) = \sum_{i=1}^{n} N_{i,p}(0) P_i = P_1 \tag{2.13}$$

$$C'(0) = \sum_{i=1}^{n} N'_{i,p}(0) P_i = \frac{p}{\xi_{p+2}} (P_2 - P_1) \tag{2.14}$$

Equation (2.13) confirms that for an open knot vector, the first control point (i.e. P_1) is interpolated at $\xi = 0$, whereas equation 2.14 shows that the curve is tangential to $\overline{P_1 P_2}$ at $\xi = 0$. The same is valid for the end of the curve, i.e. for $\xi = 1$ and the respective control points.
To summarize, the most important properties of B-Splines curves are the following:

- Convex hull property: the curve is contained inside the convex hull of the control polygon.
- In general, control points are not interpolated.
- Control points have influence on maximum $p+1$ sections.
- In case of open knot vectors, the first and last control point are interpolated; hence, the curve is tangential to the control polygon at the start and the end of the curve.
- The curve is C^{∞} continuous between two knots and C^{p-k} continuous at a knot whose multiplicity is k.
- To perform affine transformations of a B-Spline curve, its control points are transformed accordingly.

- A Bézier curve is a B-Spline curve with only one knot interval.

2.2.4 B-Splines Surfaces

A B-Splines surface is obtained by the tensor product of B-Spline basis functions in two parametric dimensions ξ and η. Therefore, given a *control net* $\{P_{i,j}\}$, $i = 1, 2, ..., n$, $j = 1, 2, ..., m$, knot vectors $\Xi = [\xi_1, \xi_2, ..., \xi_{n+p+1}]$ and $H = [\eta_1, \eta_2, ..., \eta_{m+p+1}]$ and two polynomial degrees which do not need to be equal, a tensor product B-spline surface is defined by:

$$S(\xi, \eta) = \sum_{i=1}^{n} \sum_{j=1}^{m} N_{i,p}(\xi) M_{j,q}(\eta) P_{i,j}, \tag{2.15}$$

where $N_{i,p}$ and $M_{j,q}$ are basis functions of B-Spline curves. An example of piecewise quadratic-quadratic B-Spline surface and its control net is provided in Figure (2.7).

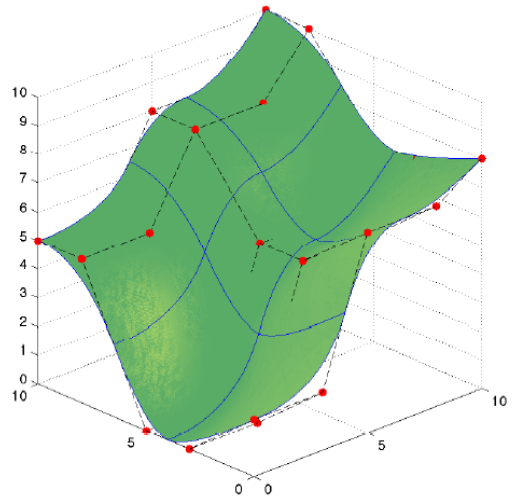

Figure 2.7: B-Spline Surface [14].

The isocurves mark the knots which partition the surface into elements. The boundaries of the surfaces are defined by the control points at the boundary and the vertices are interpolated. Many of the properties of a B-Spline surface are the result of its tensor product nature:

- The basis is pointwise nonnegative and it forms a partition of unity. Thus, $\forall(\xi, \eta) \in [\xi_1, \xi_{n+p+1}] \times [\eta_1, \eta_{m+q+1}]$,

$$S(\xi, \eta) = \sum_{i=1}^{n} \sum_{j=1}^{m} N_{i,p}(\xi) M_{j,q}(\eta) = \left(\sum_{i=1}^{n} N_{i,p}(\xi) \right) \left(\sum_{j=1}^{m} M_{j,q}(\eta) \right) = 1. \tag{2.16}$$

- The surface possesses the property of affine covariance and has a strong convex-hull property.

- The local support of basis functions follows directly from the one-dimensional functions that form them. Therefore, the support of a given bivariate function $\tilde{N}_{i,j;p,q} = N_{i,p}(\xi) M_{j,q}(\eta)$ is exactly $[\xi_i, \xi_{i+p+1}] \times [\eta_j, \eta_{j+q+1}]$.

2.2.5 B-Splines Solids

Tensor product B-spline solids are defined in analogous fashion to B-spline surfaces. In particular, given a control net $\{B_{i,j,k}\}$, i = 1,2,...,n, j = 1,2,...,m, k = 1,2,...,l, knot vectors $\Xi = [\xi_1, \xi_2, ..., \xi_{n+p+1}]$, $H = [\eta_1, \eta_2, ..., \eta_{m+q+1}]$, $Z = [\zeta_1, \zeta_2, ..., \zeta_{l+r+1}]$ and polynomial degrees p,q,r, which also in this case does not need to be equal, a B-spline solid is defined by:

$$B(\xi,\eta,\zeta) = \sum_{i=1}^{n}\sum_{j=1}^{m}\sum_{k=1}^{l} N_{i,p}(\xi)M_{j,q}(\eta)L_{k,r}(\zeta)P_{i,j,k} \tag{2.17}$$

where $N_{i,p}$, $M_{j,q}$, $L_{k,r}$ are basis functions of B-Spline curves. An example of quadratic-quadratic-linear B-spline solid is displayed in Figure (2.8).

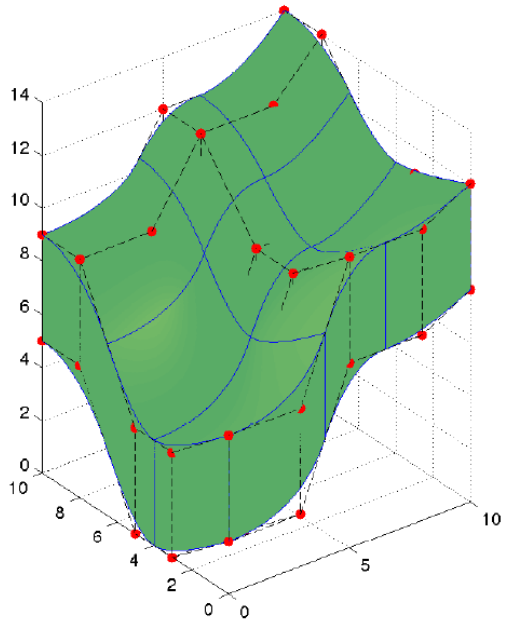

Figure 2.8: B-Spline Solid [14].

Analogous to B-Splines surfaces, the isocurves mark the knots which partition the volume into elements. The boundaries of the volume are defined by the control points at the boundary and the vertices are interpolated.
An important remark must be done: the properties of a B-Spline solid are trivariate generalizations of those of B-Spline surfaces and both of them preserve the properties of one-dimensional B-spline basis functions.

2.3 NURBS

"NURBS" is the abbreviation for Non-Uniform Rational B-Splines. The term "non-uniform" refers to the knot vector which in general is not uniform. The term "rational" refers to the basis functions. While for B-Splines the basis functions are piecewise polynomials, for NURBS they are piecewise *rational* polynomials. They were introduced because the principal drawback of using polynomials as basis functions is, including B-spline, the inability to exactly represent a wide array of geometric objects. On the contrary, NURBS significant advantage is that they allow an exact representation of conic sections, which includes circles and ellipses. Figure (2.9) shows a circle represented by NURBS. For this reason *rational* B-splines became the current standard in CAD community.
For a NURBS curve each control point has additionally to its coordinates an individual weights w_i. Such a point $P_i(x_i, y_i, z_i, w_i)$ can be represented with homogeneous coordinates $P_i^w(w_i x_i, w_i y_i, w_i z_i, w_i)$ in a projective $\mathbb{R}^4$ space. A NURBS curve is the projection of a B-Spline in $\mathbb{R}^4$ with homogeneous control points onto $\mathbb{R}^3$. To generalize, desired geometric entities in $\mathbb{R}^d$ can be obtained by projective transformations of B-splines entities in $\mathbb{R}^{d+1}$. A NURBS curve is defined as:

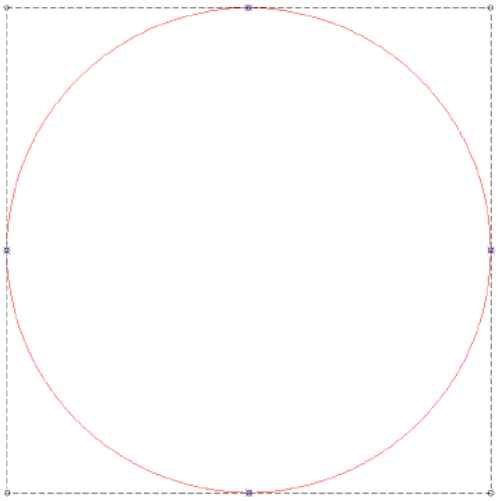

Figure 2.9: Exact circle represented by a NURBS curve.

$$C(\xi) = \frac{\sum_{i=1}^{n} N_{i,p}(\xi) w_i P_i}{\sum_{i=1}^{n} N_{i,p}(\xi) w_i} \tag{2.18}$$

If NURBS basis functions are defined as follows:

$$R_{i,p}(\xi) = \frac{N_{i,p}(\xi) w_i}{\sum_{i=1}^{n} N_{i,p}(\xi) w_i} \tag{2.19}$$

then a NURBS curve can be rewritten in the common way, i.e. the sum of control points times the respective basis functions:

$$C(\xi) = \sum_{i=1}^{n} R_{i,p}(\xi) P_i \tag{2.20}$$

If all control weights are equal, equation (2.19) reduce to equation (2.20) and so rational functions reduce to normal B-Spline functions. This means that a B-Spline is a special case of NURBS with equal control weights, but also that all properties of B-Splines listed in Section (1.1.2.3) apply to NURBS as well.
In Figure (2.10), a cubic NURBS curve is defined through the control points of the example in Figure (2.2). The "only" difference is with the increased weighting on the uppermost control point $w_5 = 10$. Due to this higher control weight, the curve is "pulled" towards this control point.
A NURBS surfaces is defined as:

$$S(\xi, \eta) = \sum_{i=1}^{n} \sum_{j=1}^{m} R_{i,j}^{p,q}(\xi, \eta) P_{i,j} \tag{2.21}$$

with the basis functions:

$$R_{i,j}^{p,q}(\xi, \eta) = \frac{N_{i,p}(\xi) M_{j,q}(\eta) w_{i,j}}{\sum_{i=1}^{n} \sum_{j=1}^{m} N_{i,p}(\xi) M_{j,q}(\eta) w_{i,j}} \tag{2.22}$$

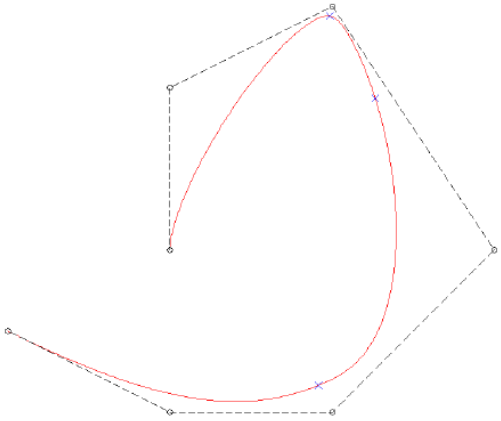

Figure 2.10: NURBS curve with increased weighting on the uppermost control point $w_5 = 10$.

A NURBS solid is defined as:

$$B(\xi,\eta,\zeta) = \sum_{i=1}^{n}\sum_{j=1}^{m}\sum_{k=1}^{l} R_{i,j,k}^{p,q,r}(\xi,\eta,\zeta)P_{i,j,k} \tag{2.23}$$

with the basis functions:

$$R_{i,j}^{p,q,r}(\xi,\eta,\zeta) = \frac{N_{i,p}(\xi)M_{j,q}(\eta)L_{k,r}(\zeta)w_{i,j,k}}{\sum_{i=1}^{n}\sum_{j=1}^{m}\sum_{k=1}^{l} N_{i,p}(\xi)M_{j,q}(\eta)L_{k,r}w_{i,j,k}} \tag{2.24}$$

One thing must be emphasized: two- and three-dimensional NURBS basis functions (equations (2.22) and (2.24) respectively) are not tensor products of one-dimensional NURBS basis functions (equation (2.19)), as seen for B-Splines: they are computed as the *weighted ratio of tensor products of B-Spline basis functions.*

2.4 Mesh Refinement

One of the most peculiar aspects of B-splines is the multiple ways in which the basis may be enriched while leaving the underlying geometry and its parameterization intact. The basic mechanisms of B-spline refinement differ from their finite element counterparts. These differences lead to more richness in the overall refinement space. In particular, both the element size and the order of the basis can be controlled together with the continuity of the basis as well.
A very important difference to refinement in classical FEA is that the refinement for B-Splines does not change the geometry. This means that in each refinement step, the geometry is represented exactly and therefore a refined mesh can be further refined without the necessity of going back to the original model.
In the following, the three IgA refinement techniques, i.e., h,p and k refinement are presented and compared, when available, with their FEA counterpart.

2.4.1 *h*-refinement: knot insertion

The first mechanism by which one can enrich the basis is *knot insertion.* In knot insertion, the knot spans are divided into smaller ones by inserting new knots without changing the curve geometrically or parametrically. For each knot inserted, an additional control point is inserted too. Also knot values already present in the knot vector may be repeated, increasing their multiplicity and reducing the

continuity at that knot location. An example of knot insertion is presented in Figure (2.11). The original curve consists of quadratic B-splines.

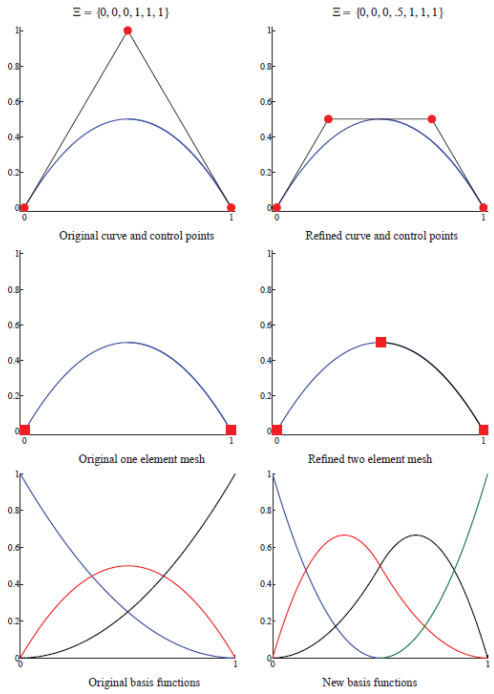

Figure 2.11: Knot insertion. Control points are denoted by •. The knots, which define a mesh by partitioning the curve into elements, are denoted by ■[7].

The knot vector is N = [0,0,0,1,1,1]. The curve is shown on the left with basis functions below. A new knot is inserted at $\bar{\xi} = 0.5$. The new curve, shown on the right, is geometrically and parametrically identical to the original curve, but the basis functions, below the curve, and control points are changed. There is one more of each. This process may be repeated to enrich the solution space by adding more basis functions of the same order while leaving the curve unchanged. This subdivision strategy is seen to be analogous to the classical h-refinement strategy in finite element analysis. It differs, however, in the lower number of new functions that are created, as well as in the continuity of the basis across the newly created element boundaries.

2.4.2 *p*-refinement: order elevation

The polynomial order of basis functions may be increased without changing the geometry or parameterization of the original structure (only the locations of control points change). In order to do this, when order p is increased, knot multiplicity k must also be increased to preserve the original C^{p-k} continuity at knot locations. Order elevation resembles the classical p-refinement strategy in FEA. The major difference is that p-refinement always begins with a basis that is C^0 everywhere, whereas order elevation is compatible with any combination of continuities that exist in the original mesh. An example of order elevation is depicted in Figure (2.12). The original curve and quadratic basis functions, shown on the left, are the same as considered in the previous example (Figure 2.11). This time the multiplicity of the knots is increased by one. The numbers of control points and basis functions each increase by one. The locations of the control points change, but the elevated curve is geometrically and parametrically identical to the original curve. There are now four cubic basis functions. The locations of control points for this elevated curve are different than those in the previous example.

2.4.3 *k*-refinement

Knot refinement and order elevation can also be combined: it is important to know that the sequence of operations is not interchangeable. While order elevation preserves all continuities, the insertion of a

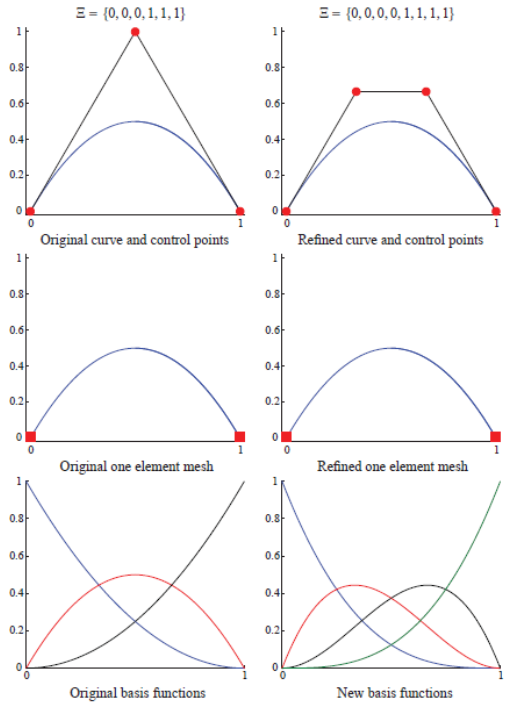

Figure 2.12: Order elevation. Control points are denoted by ●. The knots, which define a mesh by partitioning the curve into elements, are denoted by ■.[7].

knot decreases the continuity at this location. This means that performing order elevation before knot insertion yields higher continuities in the refined geometry than vice versa. In particular,

- If a unique knot ξ_i is inserted between two distinct knot values in a curve of order p, the basis will be C^{p-1} at that knot location. The order is then elevated to q, and the multiplicity of every distinct knot value (including the knot just inserted) is increased so that discontinuities of the basis are preserved. In such a process, the basis is still C^{p-1} at ξ_i but the polynomial order is now q. This process is known as *hp*-refinement.

- On the contrary, if the basis is first elevated from order p to q and subsequently knot ξ_i is inserted, the resulting basis will be C^{q-1} at knot ξ_i location. This process is referred to as k-refinement and there is no analogous technique in standard FEA.

For better understanding, a curve of polynomial degree $p = 2$ is considered. It has to be order elevated to $p = 3$ and a knot has to be inserted at a location $\bar{\xi}$. Now, the two possible aforementioned cases are considered:
Case A: *First*, order elevation is performed, the polynomial degree is now p = 3. *Then*, the knot is inserted. The continuity at this knot is $C^{p-k} = C^{3-1} = C^2$.
Case B: *First*, the knot is inserted. The continuity at this knot is then $C^{p-k} = C^{2-1} = C^1$. *Then*, order elevation is performed. Since order elevation preserves all continuities, the continuity at $\bar{\xi}$ remains C^1. Unless low continuities are desired, order elevation is always performed before knot insertion (thus, k-refinement is always preferred to hp-refinement).

2.5 NURBS-based Isgeometric Analysis

As stated before, NURBS are not a requisite ingredient in isogeometric analysis. Isogeometric procedures may be developed based on all functions used in computer aided design, provided that they fulfill the necessary conditions for basis functions, such as linear independence and partition of unity. Since NURBS are the most widespread technology in today's CAD programs and they fulfill the necessary

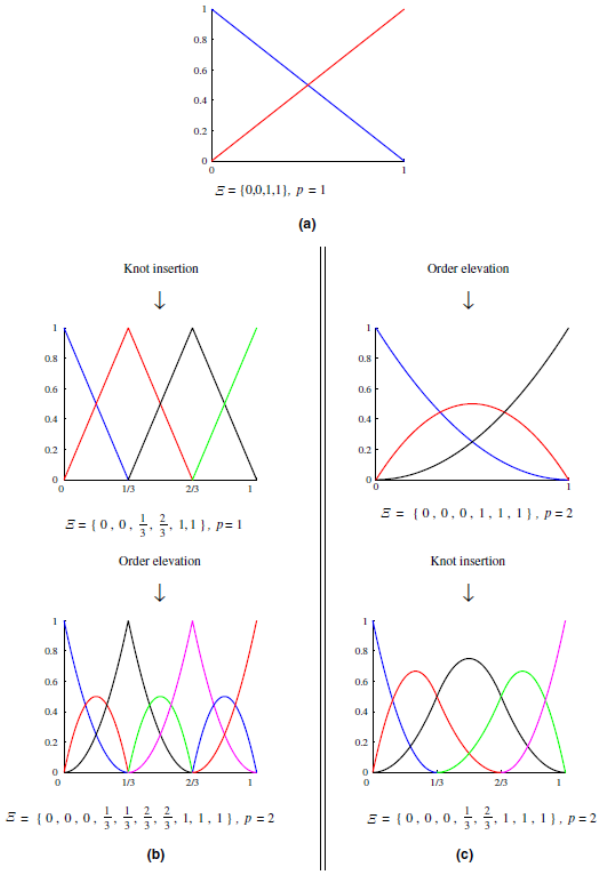

Figure 2.13: k-refinement takes advantage of the fact that knot insertion and order elevation do not commute. (a) Base case of one linear element. (b) Classic p-refinement approach: knot insertion followed by order elevation results in seven piecewise quadratic basis functions that are C^0 at internal knots. (c) New k-refinement approach: order elevation followed by knot insertion results in five piecewise quadratic basis functions that are C^1 at internal knots [7].

conditions mentioned above, for this reason they are adopted for analysis. Isogeometric analysis works with elements as its finite element counterpart. There are two possible definitions of an element:

- NURBS elements are defined by the knot spans of the knot vectors. This means that the domain consists of a couple of NURBS patches and each patch plays the role of subdomain within which element types and material models are assumed to be uniform.
- The whole patch is considered as one NURBS element.

In what follows, the definitions for isogeometric NURBS-elements are presented, as well as their consequences for analysis and the differences to classical finite element analysis.

2.5.1 Elements

A NURBS patch is defined over a parametric domain: it is divided into intervals by the knot vectors. These intervals are defined as elements. This because inside a knot interval, B-Spline basis functions are polynomials and therefore Gauss quadrature can be used for integration on element level. NURBS basis functions are not polynomials but rational polynomials. Therefore, the integration with Gauss quadrature is only approximative for NURBS basis functions. But it is important to remind that not the basis functions per se are integrated, but the element formulation, which in general results in the integration of rational polynomials anyhow. A NURBS element is defined by a set of nodes and corresponding basis functions. The nodes are the NURBS control points. This is equivalent to finite

elements analysis. They carry the degrees of freedom for the analysis and boundary conditions are applied to them. The element formulation adopted in this thesis is displacement-based: therefore, the degrees of freedom are the displacements of the control points. For three-dimensional structures this means that every control point has three degrees of freedom, namely the displacements in x-, y- and z-direction. With this definition of elements, the basis functions are not confined to one element but extend over a series of elements, as illustrated in Figure (2.14).

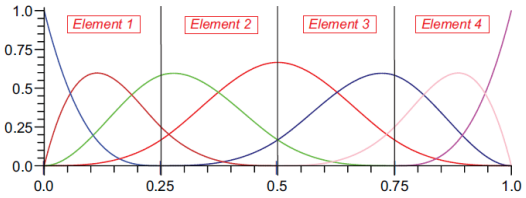

Figure 2.14: Isogeometric elements: The basis functions extend over a series of elements [22].

This is a very important difference to classical finite elements because it allows higher continuities of shape functions over the element boundaries, i.e. between elements. It also means that elements are interconnected and not independent of each other. The basis functions inside a knot span are defined by the Cox-deBoor recursion formula and depend on the neighboring knot spans, as seen in (2.4). Therefore, it is not possible to define a single NURBS element without a complete NURBS patch. With regard to the computational implementation, these elements can be treated exactly in the same way as classical finite elements. The stiffness matrix, for example, is evaluated on element level and assembled to the global stiffness matrix. What changes is the use of different shape functions. The fact that the corresponding nodes, i.e. control points, usually lie outside the element, is solely a consequence of the used basis functions and does not make any difference in the treatment of these elements in a finite element code.

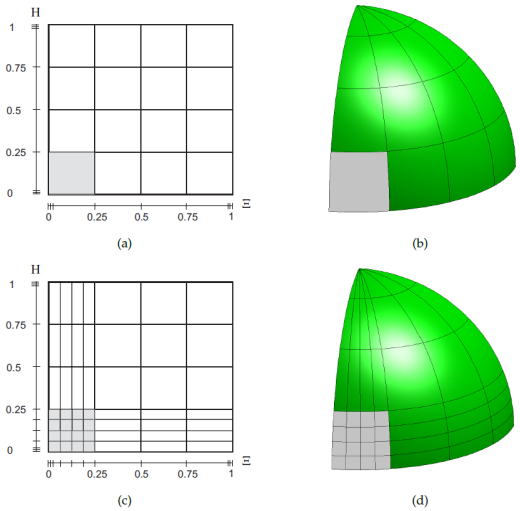

Figure 2.15: (a) Unrefined parametric space. (b) Unrefined physical model. (c) Refined parametric space. (d) Refined physical model. Element is highlighted [22].

One last concept must be expressed. Mesh refinement was introduced for B-Splines: all the previously mentioned techniques can be applied to NURBS curves, surfaces and solids as well, according to the desired results (their properties still hold also in these cases). As before, refinement for NURBS does not change the geometry: in each refinement step, the geometry is represented exactly and therefore a refined mesh can be further refined without the necessity of going back to the original model. Knot refinement can be used to refine a NURBS curve and knots can be inserted arbitrarily. This means that

local refinement for a NURBS curve is possible. In case of NURBS surfaces, however, knot insertion can be applied but a knot inserted in the ξ-direction extends over the whole patch in the η-direction and viceversa. This is shown in Figure (2.15): As a consequence, "pure" local refinement is not possible for NURBS. The same holds for NURBS solids. The reason for this is the tensor product structure of NURBS surfaces. An alternative could be the use of T-Splines, which are not confined to a tensor product structure.

Chapter 3

Structural Mechanics of shells

In this chapter, the fundamentals of continuum mechanics are reviewed ([37]). The most important kinematic equations are derived. They are based on the principal quantities of differential geometry presented in chapter (4). In particular, large displacements and small strains are assumed and a Lagrangian description is used. Afterwards, Kirchoff-Love shell theory is described (for a full dissertation regarding shell formulation please refer to [22]).

3.1 Kinematics

Consider a body as a set of material points: kinematics investigates its deformation. Given one of its material points, the difference between reference (i.e. undeformed) and actual (i.e. deformed) configuration must be taken into account. The following rule has been used throughout this work: all quantities in the reference configuration are denoted by upper case letter, whereas those referred to the actual configuration by lower case letters.
The deformation **u** of a material point is defined by its position vectors in the actual and reference configuration. They are both vectorial fields. In particular,

$$u = x - X \tag{3.1}$$

The second order tensor which describes the mapping from the reference to the actual configuration is the deformation gradient "F". It is a key measure in finite deformation analysis and it is involved in all equations relating quantities before deformation to corresponding quantities after (or during) deformation. It enables the relative spatial position of two neighboring particles to be described in terms of their relative material positions before deformation; thus it is central to the description of deformation and hence strain.
Given that dx and dX are the differential position vectors in the actual and reference configuration, respectively, dx is computed through F by:

$$dx = F \cdot dX \tag{3.2}$$

This means that F transforms vectors in the initial or reference configuration into vectors in the current configuration. Therefore it is said to be a *two-point* tensor. By expressing the motion in function of time and the position vector in reference configuration as:

$$x = x(X, t) \tag{3.3}$$

the deformation gradient tensor can be written in a clearer way as:

$$F = \frac{\partial x}{\partial X} \tag{3.4}$$

It can also be characterized by base vectors in the reference and actual configuration:

$$F = g_i \otimes G^i \qquad F^T = G^i \otimes g_i \tag{3.5}$$
$$F^{-1} = G_i \otimes g^i \qquad F^{-T} = g^i \otimes G_i \tag{3.6}$$

and it can be used for the mapping between deformed and undeformed base vectors:

$$g_i = F \cdot G_i \qquad G_i = F^{-1} \cdot g_i \tag{3.7}$$
$$g^i = F \cdot G^i \qquad G^i = F^T \cdot g^i \tag{3.8}$$

The deformation gradient describes the deformation of a body including rigid body motions. In particular, it considers not only deformations, but also rotations (i.e changes in the enclosed angle between two vectors) and stretches (i.e. changes in length). Therefore, it cannot be used as a direct measure for strains. Many strain measures exist: the one here considered is "E", the Green-Lagrange strain tensor.

$$E = \frac{1}{2}(F^T \cdot F - I) = E_{ij} G^i \otimes G^j \tag{3.9}$$

It is an appropriate measure for strains under large deformations, since it describes a non linear relation between deformations and strains. In particular, in case of undeformed body (i.e. when zero deformations occur) $F^T \cdot F = I$, thus E is equal to zero according to (3.9), differently from other possible strain measures: for example, "C", the right Cauchy-Green strain tensor, defined as $F^T \cdot F$, in case of undeformed body consists of the identity matrix I. Inserting equations (3.5) and (3.6) into (3.9) and recalling that the identity tensor is identical to the metric tensor (as in 4.9), yields:

$$\begin{aligned} E &= \frac{1}{2}((G^i \otimes g_i) \cdot (g_i \otimes G^i) - G_{ij} G^i \otimes G^j) \\ &= \frac{1}{2}(g_{ij} - G_{ij}) G^i \otimes G^j \end{aligned} \tag{3.10}$$

Directly from (3.10), the Green-Lagrange strain coefficients E_{ij} can be derived. They are:

$$E_{ij} = \frac{1}{2}(g_{ij} - Gij) \tag{3.11}$$

and they refer to the contravariant basis $G^i \otimes G^j$ of the undeformed configuration.

3.2 Constitutive Equations

The constitutive equations describe the relation between strains and stresses via a material law. As with strain tensor, there exist different definitions of stress tensors. The energetically conjugated quantity to the Green-Lagrange strain tensor E is the *second* Piola-Kirchhoff stress tensor "S" (in the following indicated as PK2). Differently from the *first* Piola-Kirchhoff tensor P (PK1) that is an unsymmetric two-point tensor and as such is not completely related to the material configuration, S is totally material and symmetric. S can be computed from the strain energy W^{int} as:

$$S = \frac{\partial W^{int}}{\partial E} \tag{3.12}$$

Stress and strain tensor are related by the elasticity fourth order tensor C, also called *Lagrangian* or *material elasticity tensor*:

$$C = \frac{\partial S}{\partial E} = \frac{\partial^2 W^{int}}{\partial E^2} \tag{3.13}$$

Depending from the material model used, the relation between stress and strains can be linear. For instance, by considering the simplest example of an hyperelastic material model, commonly known as

"St.Venant-Kirchhoff" model, for which the expression of the second Piola-Kirchhoff stress tensor is given by:

$$S = \lambda(trE)I + 2\mu E \tag{3.14}$$

whereas the coefficients of the Lagrangian elasticity tensor are,

$$C_{IJKL} = \lambda\delta_{IJ}\delta_{KL} + 2\mu\delta_{IK}\delta_{JL} \tag{3.15}$$

the following formulas hold:

$$S = C : E \tag{3.16}$$

$$S^{ij} = C^{ijkl}E_{kl} \tag{3.17}$$

$$S = S^{ij}G_i \otimes G_j \tag{3.18}$$

In equation (3.15) two independent parameters have been introduced: λ and μ. They are called "Lamé constants" and they are sufficient to describe an isotropic elastic material. Isotropy is defined by requiring the constitutive behavior to be identical in any material direction. These constants are connected to Young's modulus E and Poisson's ratio ν by:

$$\lambda = \frac{E\nu}{(1+nu)(1-2\nu)} \quad \mu = \frac{E}{2(1+\nu)} \tag{3.19}$$

As stated before, the second Piola-Kirchhoff stress tensor S is the energetically conjugate to the Green-Lagrange strain tensor. However, it does not represent physical stresses. Those are described by the Cauchy stress tensor σ. The Cauchy and the PK2 stress tensor are related by the deformation gradient F as follows:

$$\sigma = (detF)^{-1} \cdot F \cdot S \cdot F^T \tag{3.20}$$

$$S = detF \cdot F^{-1} \cdot \sigma \cdot F^{-T} \tag{3.21}$$

The first Piola-Kirchhoff (PK1) stress tensor can be obtained in analogous fashion as (3.21) by:

$$P = det(F) \cdot \sigma \cdot F^{-T} = F \cdot S \tag{3.22}$$

3.3 Equilibrium

The equilibrium equations describe the balance between internal and external forces. If those equations are satisfied, the system is in equilibrium. In the reference configuration, the equilibrium is formulated as:

$$divP + \rho_0 B = div(F \cdot S) + \rho_0 B = 0 \tag{3.23}$$

where ρ_0 is the density and B the vector of body forces, both referred to reference configuration. The strong form of the boundary value problem is represented through equations (3.10), (3.12) and (3.23), together with the appropriate boundary conditions. For general three dimensional problems, the strong form of the problem can not be solved exactly; therefore discretization methods, like the Finite Element Method, must be employed. According to it, the field equations and boundary conditions are not satisfied point-wise but only in integral sense. The resulting equation of equilibrium is called the weak form of the problem. Since the finite element formulation is established in terms of the weak form of the differential equations under consideration, in the context of solid mechanics this implies the use of the Principle of Virtual Work or, to be more precise, the Principle of Virtual Displacements. It states that if an infinite small virtual displacement δu is applied to a system, the sum of internal and external work, done by the internal and external forces on the virtual displacement, vanishes if

the system is in equilibrium:

$$\partial W = \partial W_{int} + \partial W_{ext} = 0 \tag{3.24}$$

The internal and external work are defined as:

$$\delta W_{int} = -\int_{\Omega} \delta E : S \, d\Omega \tag{3.25}$$

$$\delta W_{ext} = \int_{\Gamma} T \cdot \delta u \, d\Gamma + \int_{\Omega} \rho B \cdot \delta u \, d\Omega \tag{3.26}$$

where Ω is the domain and Γ the domain boundary in the reference configuration and T is the vector of boundary forces.

3.4 Kirchhoff-Love shell theory

The Kirchhoff-Love shell theory is a shell theory based on the "direct" approach (for a comprehensive review of the different approaches to shell theories, reference is made to[4]). It means that the shell formulation is not derived from three-dimensional continuum mechanics, but the shell itself is regarded ab initio as a two-dimensional surface and proper kinematic assumptions, regarding the three-dimensional behavior, are postulated.
To fully understand how this element is and works, the following points and some practical issues must be taken into account:

- It is a three-dimensional element but it is treated as a bi-dimensional one. It consists of a top, a middle (or reference) and a bottom surface, the three of them defining together the thickness of the element. The thickness might not be constant throughout the element: as a matter of fact, the director, which is a vector field on the shell's middle surface, describes point per point the thickness extension of the shell. Moreover, being a three-dimensional entity regarded as a bi-dimensional one means that when modeling something which consists of shell elements, the third dimension must not be considered and thus modeled: the thickness is intrinsic in element formulation.

- In the Kirchoff-Love shell theory, cross sections are assumed to remain straight during deformation, which corresponds to a linear strain distribution through the thickness. Furthermore, it assumes that cross sections that are normal to the middle surface remain normal to the middle surface in the deformed configuration. From the latter, the following concept can be derived: the shell can be completely represented by its middle surface.

- Shell elements based on the Kirchhoff-Love theory are regarded as thin shell. A thin shell is defined by a slenderness of $\frac{R}{t} > 20$, where R is the radius of curvature and t the shell's thickness. Otherwise the shell is defined as thick. Thick shell are described by the Reissner-Mindlin theory (not considered in this work): the difference between the two is that while the Reissner-Mindlin theory does take into account transverse shear deformations, Kirchhoff-Love one does not. Mechanically, the fact that transverse shear strains are neglected for the Kirchhoff-Love shells equals the assumption that cross sections remain normal to the midsurface during deformation.

- Another extremely important difference between Reissner-Mindlin and Kirchhoff-Love theory, is the following: Reissner-Mindlin shell theory requires only C^0 continuity and treats rotations and deflections as two independent fields. On the other hand, Kirchhoff-Love shell theory requires integrability of second derivatives and therefore at least C^1 continuity is required and no rotations are taken into account. Hence, Finite Element Analysis can be used with Reissner-Mindlin theory because it succeeds in guaranteeing C^0 continuity between elements, but it prohibits a straight-

forward use of Kirchhoff-Love shell theory since this one demands at least C^1 continuity between elements.

In the next section, the previous assumptions are applied to kinematic, constitutive, and equilibrium equations previously introduced.
As said before, both transversal normal strains and transversal shear strains are neglected. Therefore, only the in-plane strain coefficients are considered. Thus, equation (3.9) becomes:

$$E = E_{\alpha\beta} G^{\alpha} \otimes G^{\beta} \tag{3.27}$$

Strain coefficient $E_{\alpha\beta}$ are defined as:

$$E_{\alpha\beta} = \frac{1}{2}(g_{\alpha\beta} - G_{\alpha\beta}) \tag{3.28}$$

according to equation (3.11). Due to the fact that cross sections remain straight during deformation, a point in the shell continuum can be described by the middle surface and its normal vector. Denoting t as the shell thickness and θ^3 as the thickness coordinate ranging from $(-0.5 \leq \theta^3 \leq 0.5)$, then all those points for which $\mathrm{x}(\theta^3 = 0)$ define the middle surface. Orthonormal basis vectors on the middle surface are computed by:

$$a_{\alpha} = x_{,\alpha}(\theta^3 = 0) \tag{3.29}$$

$$a_3 = \frac{a_1 \times a_2}{|a_1 \times a_2|} \tag{3.30}$$

Metric and curvature coefficients of the middle surface are defined by:

$$a_{\alpha\beta} = a_{\alpha} \cdot a_{\beta} \tag{3.31}$$

$$b_{\alpha\beta} = -a_{\alpha} \cdot a_{3,\beta} = -a_{\beta} \cdot a_{3,\alpha} = a_{\alpha,\beta} \cdot a_3 \tag{3.32}$$

analogously to (4.14).
The position vector x of a generic point *in the shell continuum* is given by:

$$x = \theta^{\alpha} a_{\alpha} + \theta^3 a_3 \tag{3.33}$$

which yields for the base vectors g_{α},

$$g_{\alpha} = a_{\alpha} + \theta^3 a_{3,\alpha} \tag{3.34}$$

and for the metric coefficients $g_{\alpha\beta}$:

$$g_{\alpha\beta} = g_{alpha} \cdot g_{\beta} \tag{3.35}$$

Inserting equation (3.34) into equation (3.35) and recalling equation (3.32) gives:

$$\begin{aligned} g_{\alpha\beta} &= (a_{\alpha} + \theta^3 a_{3,\alpha}) \cdot (a_{\beta} + \theta^3 a_{3,\beta}) \\ &= a_{\alpha\beta} + a_{\beta}\theta^3 a_{3,\alpha} + a_{\alpha}\theta^3 a_{3,\beta} + (\theta^3)^2 a_{3,\alpha} a_{3,\beta} \\ &= a_{\alpha\beta} - 2\theta^3 b_{\alpha\beta} + (\theta^3)^2 a_{3,\alpha} \cdot a_{3,\beta} \end{aligned} \tag{3.36}$$

The quadratic term with respect to θ^3 in (3.36) can be neglected for thin and moderately thick shells. This results in:

$$g_{\alpha\beta} = a_{\alpha\beta} - 2\theta^3 b_{\alpha\beta} \tag{3.37}$$

By inserting equation (3.37) into equation 3.28, the strain coefficients $E_{\alpha\beta}$ can be derived:

$$E_{\alpha\beta} = \frac{1}{2}(a_{\alpha\beta} - A_{\alpha\beta}) + \theta^3(B_{\alpha\beta} - b_{\alpha\beta}) \tag{3.38}$$

Hence, the strain in the shell continuum are represented by metric and curvature coefficients of the middle surface. Equation (3.38) can be further specified: it consists of two parts, a constant and a linear one. The constant part is the first one and describes the strains in the middle surface. It corresponds to membrane action (membrane are derived from the shell elements by deleting the bending and shearing deformations, thus leaving only the in-plane strain deformation terms). Membrane strains can be defined as:

$$\epsilon_{\alpha\beta} = \frac{1}{2}(a_{\alpha\beta} - A_{\alpha\beta}) \tag{3.39}$$

The second part is linear and symmetric with respect to the middle surface (because $-0.5 \leq \theta^3 \leq 0.5$ holds). It represents the change in curvature and it is the effect of bending. The change in curvature is defined by:

$$k_{\alpha\beta} = B_{\alpha\beta} - b_{\alpha\beta} \tag{3.40}$$

Taking into account (3.39) and (3.40), equation (3.38) can be rewritten as:

$$E_{\alpha\beta} = \epsilon_{\alpha\beta} + \theta^3 k_{\alpha\beta} \tag{3.41}$$

Once computing the strains, stresses can be derived. The separation into membrane and bending action can be applied also to stresses. If an integration through the thickness is performed, the stress resultants $\mathbf{n}$ for normal forces and $\mathbf{m}$ for bending moments are obtained. Since the stress distribution through the thickness is defined to be linear, a pre-integration can be performed analytically:

$$S^{\alpha\beta} = C^{\alpha\beta\gamma\delta} E_{\gamma\delta} \tag{3.42}$$

$$S^{\alpha\beta} = \int_{-t/2}^{t/2} S^{\alpha\beta} d\theta^3 = C^{\alpha\beta\gamma\delta} \epsilon_{\gamma\delta} \cdot t \tag{3.43}$$

$$S^{\alpha\beta} = \int_{-t/2}^{t/2} S^{\alpha\beta} \theta^3 d\theta^3 = C^{\alpha\beta\gamma\delta} k_{\gamma\delta} \cdot \frac{t^3}{12} \tag{3.44}$$

Since both strains and stresses are symmetric, only three independent components exist. They are E_{11}, E_{22}, E_{12} for strains and S^{11}, S^{22}, S^{12} for stresses. By representing them in column vectors, the constitutive equation can be written in Voigt notation:

$$\begin{bmatrix} S^{11} \\ S^{22} \\ S^{12} \end{bmatrix} = \tilde{D} \cdot \begin{bmatrix} E_{11} \\ E_{22} \\ 2E_{12} \end{bmatrix} \tag{3.45}$$

where $\tilde{D}$ is the material matrix. Usually, the material matrix is built using physical material parameters like the Young's modulus E. Since these quantities refer to normalized units (like m or mm), the strains and stresses in equation (3.42) need to be expressed in a local Cartesian coordinate system. The following rule can be used to transform strain coefficients from $E_{\alpha\beta}$ to $\bar{E}_{\alpha\beta}$, where the upper bar signifies that these coefficients refer to a local Cartesian basis:

$$b_{kl} = a_{ij}(b_k \cdot a^i)(a^j \cdot b_l) \tag{3.46}$$

By using equation (3.46), $E_{\alpha\beta}$ are transformed into $\bar{E}_{\alpha\beta}$:

$$\bar{E}_{\gamma\delta} = E_{\alpha\beta}(E_\gamma \cdot G^\beta)(G^\beta \cdot E_\delta) \tag{3.47}$$

The local base vectors E_γ and E_δ can be obtained by using:

$$e_1 = \frac{g_1}{\|g_1\|} \tag{3.48}$$

and

$$e_2 = \frac{g_2 - (g_2 \cdot e_1)e_1}{\|g_2 - (g_2 \cdot e_1)e_1\|} \tag{3.49}$$

Since the local Cartesian base is an orthogonal and normalized basis with an arbitrary orientation, it has been defined such that its first base vector e_1 (i.e. E_γ) is parallel to g1, and e_2 (i.e. E_δ) is orthogonal to it, lying in the plane of g_1 and g_2. The new base vectors are denoted with capital letters, since they refer to the reference configuration. A material matrix D using physical components can be used to compute the PK2 stress coefficients $\bar{S}_{ab}$. As for the strains, the upper bar notation refers to a local Cartesian basis:

$$\begin{bmatrix} \bar{S}^{11} \\ \bar{S}^{22} \\ \bar{S}^{12} \end{bmatrix} = D \cdot \begin{bmatrix} \bar{E}_{11} \\ \bar{E}_{22} \\ 2\bar{E}_{12} \end{bmatrix} \tag{3.50}$$

If the material is isotropic, the material matrix D takes on the following expression:

$$D^{iso} = \frac{E}{1-\nu^2} \begin{bmatrix} 1 & \nu & 0 \\ \nu & 1 & 0 \\ 0 & 0 & \frac{1-\nu}{2} \end{bmatrix} \tag{3.51}$$

with E as the Young's modulus and ν as the Poisson's ratio. Tensor n and m are also symmetric and can be computed using material matrix D and Voigt location, as in (3.45). The bar over the coefficients again refers to a local Cartesian basis:

$$\begin{bmatrix} \bar{n}^{11} \\ \bar{n}^{22} \\ \bar{n}^{12} \end{bmatrix} = t \cdot D \cdot \begin{bmatrix} \bar{\epsilon}_{11} \\ \bar{\epsilon}_{22} \\ 2\bar{\epsilon}_{12} \end{bmatrix} \tag{3.52}$$

$$\begin{bmatrix} \bar{m}^{11} \\ \bar{m}^{22} \\ \bar{m}^{12} \end{bmatrix} = \frac{t^3}{12} \cdot D \cdot \begin{bmatrix} \bar{k}_{11} \\ \bar{k}_{22} \\ 2\bar{k}_{12} \end{bmatrix} \tag{3.53}$$

With normal forces and bending moments, internal virtual work can be rewritten as:

$$\delta W = -\int_\Omega (S : \delta E) d\Omega = -\int_A (n : \delta\epsilon + m : \delta k) dA \tag{3.54}$$

where dA is the differential area of the midsurface in the reference configuration. Equation (3.54) represents a weak form of the partial differential equations for the Kirchhoff-Love shell. In the next section, these equations are derived for a discretized system.

3.5 NURBS-based Kirchhoff Love shell

The formulation here presented is valid for a displacement-based formulation of Kirchhoff-Love theory and is not specific to NURBS. Using a NURBS discretization has the advantage to provide an exact description of the surface and therefore all metric quantities can be evaluated without further assumptions. The variational variables are the nodal displacements variables.

Recalling the Principle of Virtual Work previously introduced in (3.24), it states an equilibrium

condition that must be fulfilled for any arbitrary variation of displacement variables δu_r:

$$\delta W = \frac{\partial W}{\partial u_r}\delta u_r = 0 \tag{3.55}$$

$$\frac{\partial W}{\partial u_r} = 0 \tag{3.56}$$

Equation 3.56 represents a non linear equation system that is linearized in order to solve it. For solving the linearized equation system the Newton-Raphson method is used.
The virtual work is defined as the sum of internal and external virtual work (3.24). The internal virtual work was formulated in equation (3.54). For the sake of clarity, it is here repeated for a better understanding of the following formulas:

$$\delta W_{int} = -\int_A (n : \delta\epsilon + m : \delta k) dA \tag{3.57}$$

Taking the first derivative of the virtual work w.r.t a displacement variable yields the residual force vector R:

$$R_r = (\frac{\partial W_{int}}{\partial u_r} + \frac{\partial W_{ext}}{\partial u_r}) = F_r^{int} + F_r^{ext} \tag{3.58}$$

In equation 3.58 F^{ext} is the vector of external nodal loads and F^{int} the vector of internal nodal forces:

$$F_r^{int} = -\int_A (n : \frac{\partial \epsilon}{\partial u_r} + m : \frac{\partial k}{\partial u_r})\ dA \tag{3.59}$$

The second derivatives of the virtual work yield the stiffness matrix. Splitting into internal and external virtual work, the stiffness matrix K is:

$$K_{rs} = -(\frac{\partial^2 W_{int}}{\partial_r \partial u_s} + \frac{\partial^2 W_{ext}}{\partial_r \partial u_s}) = K_{rs}^{int} + K_{rs}^{ext} \tag{3.60}$$

The "external" stiffness matrix K^{ext} is computed by taking the second derivative of the external loads w.r.t the displacement variables: thus, it is considered only in the case of displacement-dependent loads.
On the other hand, the "internal" stiffness matrix is obtained by deriving the term of the internal virtual work w.r.t. the displacement variables. This means solving the following integral:

$$K_{rs}^{int} = \int_A (\frac{\partial n}{\partial u_s} : \frac{\partial \epsilon}{\partial u_r} + n : \frac{\partial^2 \epsilon}{\partial u_r \partial u_s} + \frac{\partial m}{\partial u_s} : \frac{\partial k}{\partial u_r} + m : \frac{\partial^2 k}{\partial u_r \partial u_s})\ dA \tag{3.61}$$

The first two terms represent the membrane stiffness and the latter two the bending stiffness. A remark needs to be done: in a discretized system with n nodes where $\hat{u}_i$, i = 1,...,n, are the discrete nodal displacement vectors and N^i the corresponding shape functions, the first derivatives of the covariant base vectors w.r.t. the displacement variables u_r are given by:

$$\frac{\partial g_\alpha}{\partial u_r} = \frac{\partial (X_{,\alpha} + u_{,\alpha})}{\partial u_r} = \frac{\partial u_{,\alpha}}{\partial u_r} = \sum_{i=1}^{n} N_{,\alpha}^i \frac{\partial \hat{u}_i}{\partial u_r} \tag{3.62}$$

Starting from Equation (3.62), the derivatives of ϵ, k, n and m w.r.t the displacement variables u_r can be taken in the same way.

Chapter 4

Isogeometric large deformation frictionless contact using NURBS

In this chapter, the NURBS-based isogeometric paradigm to frictionless contact analysis in the context of large deformations is presented.
Within this framework, NURBS is used to discretize the continuum and for analysis, whereas a Gauss-point-to-surface formulation is combined with the penalty method to treat the contact constraints in the discretized setting.
Differences between the traditional FE and NURBS-based approach to contact analysis are also pointed out.

4.1 NURBS vs FE contact analysis

4.1.1 Basis concepts of computational contact mechanics

Contact analysis is one of the most difficult tasks in computational mechanics: this because contact interactions are not only non-linear but also non-smooth. They are non-linear because contact conditions introduces additional kinematics constraints to prevent compenetration between the two bodies. Furthermore, they are non-smooth because of the physical nature of the problem, together with the geometric discontinuities induced by spatial discretization.
Along the boundary Γ_c of two bodies 4.1, different contact models can be investigated: in this work, the *frictionless* contact has been used. It is the simplest one and the only non-zero component of the contact traction vector is the one *normal* to the contact surfaces. Traditional FE based contact analysis has been widely employed for many years. *Contact pairs* are the key entities in computational contact mechanics. They are valid both for the FE approach and for the isogeometric one. They are a couple of points, one for the master and one for the slave body, where contact constraints are locally enforced. They can be defined in multiple ways, such as:

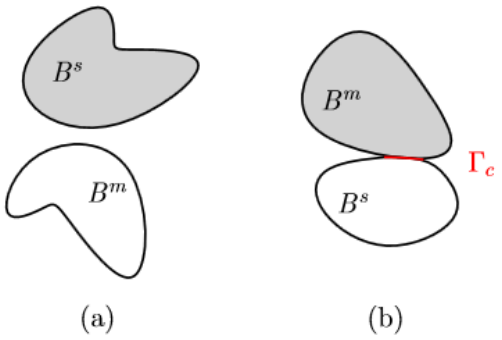

Figure 4.1: 2D Contact Problem. (a) no contact; (b) contact state [14]

- *Node-to-Node contact*: it is the most constraining approach because two mesh nodes must be selected, one coming from the slave and the other from the master body. It proves to be satisfactory only in geometrically linear cases and only if the two meshes along the contact surface Γ_c matches. In general, nodes at the contact interfaces are located at different coordinates: therefore, node-to-node algorithms sometimes cannot be used even in geometrically linear cases.

- *Node-to-segment contact*: it is the method that has been used in this thesis; each contact pair is defined by a node coming from the *slave* surface and its projection on the *master* surface, that not necessarily coincides with a node. Given the pairs, the gap g determines which nodes are in contact. This quantity is defined by:

$$g = (x^s - x^m)n_c \tag{4.1}$$

  where x^s is the slave node, and x^m the *location* of its projection onto the deformed master surface. n_c is the outward normal evaluated at the projection point: it relies on the deformed configuration too. Using g, the relative position between the two bodies can be deduced: as a matter of fact, if $g > 0$ there is no contact, whereas if $g < 0$ compenetration occurs.
  Given that the total energy of a system is usually indicated as Π, in this case, a proper contact contribution Π_c must be considered when contact occurs. Π_c can be written in different forms according to different techniques; in this thesis the one that goes under the name of *penalty function form* is the one that has been employed:

$$\Pi_c = \Pi(u) = \int_{\Gamma_c} \epsilon g^2 d\Gamma. \tag{4.2}$$

  In equation (4.2) ϵ is a positive, user-defined, penalty coefficient. This formulation allows for some small compenetration controlled by the parameter ϵ: this means that *the final gap is not zero*, but it can be reduced with higher values of ϵ. Its principal drawback is that no general rule exists to identify a proper value of ϵ.

In this work, the isogeometric framework is used, not the FE one. Specifically, the isogeometric approach with NURBS as smooth parametric geometry. We used NURBS because NURBS-based analysis has some distinct features, that can help to overcome several problems the FE-based analysis still has. For example, NURBS geometry preserves geometric continuity: this property is fundamental to address the numerical issues related to the geometric discontinuities that come from discretization. Moreover, with NURBS geometry, continuity can be flexibly controlled by selecting the appropriate NURBS basis and surface representation are intrinsically smooth, which means that no smoothing operations is required and so computation overhead is prevented.

4.2 Knot-to-segment contact formulation: toward an IgA based approach

Nowadays the most implemented technique for FEA contact problems is the node-to-segment approach (Figure 4.2). Several numerical problems in the geometric description of the contact surfaces may occur if non-smooth and facet-based contact routines are used. The non uniqueness of the master projection is the principal drawback of these problems. Table 4.1 is aimed at better illustrating this issue by providing two examples.

The previous matters are strictly related to:

- FEA not-smooth geometric description of the contact surfaces;

- C^0 continuity along the inter element FEA nodes.

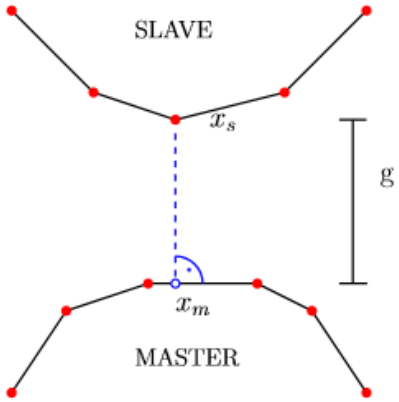

Figure 4.2: Node-to-segment contact [14]

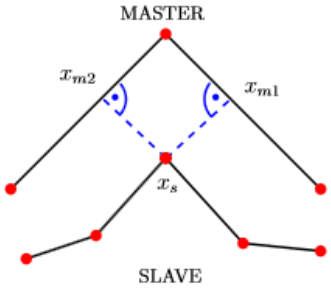	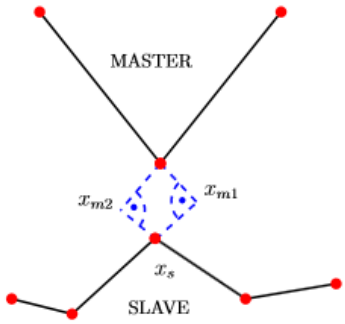
Two projections on the master side	No projections on the master side

Table 4.1: Non uniqueness of the master projection: two possible cases [14].

Given the prior statements, IgA seems to be naturally able to provide an ideal framework to overcome these issues in terms of surface smoothness. The NTS approach can not be directly extended to IgA due to the non-interpolatory nature of the control points. This limitation has been overcome by Temizer et al. [21] by proposing the "Knot-to-segment" approach, in which the contact constraint is not imposed on slave nodes but at the Gauss points belonging to each slave contact surface (Figure 4.3).

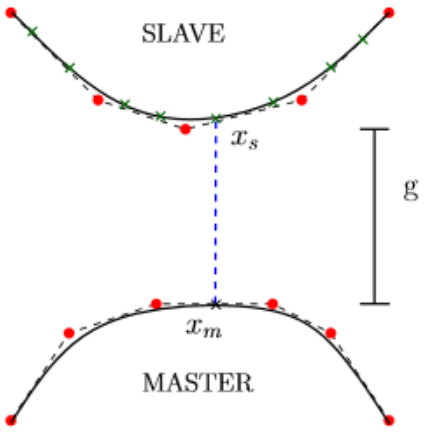

Figure 4.3: Knot-to-segment contact. Gauss points on slave contact surface are highlighted in green color. [14]

According to Temizer and colleagues, the first implementation of the KTS algorithm performed better

than NTS in terms of quality and robustness. At the same time, they pointed out that the KTS implementation leads to an over-constrained problem induced by the discrepancy between the total number of degrees of freedom of the contact surfaces and the number of contact pairs, e.g. the number of Gauss points. Moving from these considerations, two different approaches have been proposed in order to relax the over-constrained formulation:

- A mortar based KTS method has been implemented by Temizer et al. [21] and by De Lorenzis et al.[24]. This KTS formulation performed better than classic KTS and NTS.
- Following an already successfully implemented technique in NURBS collocation methods [12], Matzen et al.[28] proposed to collocate the contact constraint on particular points e.g., Greville and Botella points. The use of Greville and Botella points gives a consistent number of collocation points along with the control points on the contact surface.

4.3 NURBS-based Contact Description

This section summarizes the theoretical and algorithmic background of the normal contact between two deformable bodies undergoing finite deformations ([44]). Firstly, the basics of the differential geometry of surfaces are reviewed (see section 4.3.1). They are fundamental to understand the geometry of normal contact, depicted in section (4.3.2).

4.3.1 Differential Geometry of Surfaces

Consider a point in the three dimensional space; it can be identified by its position vector $\mathbf{x}$:

$$x = x^1 e_1 + x^2 e_2 + x^3 e_3 = x^i e_i \tag{4.3}$$

where e_i are the global Cartesian base vectors and x^i its coordinates. The Einstein summation convention is used throughout this chapter as well as the convention that indices in Latin letters take the values {1,2,3}, whereas indices in Greek letters take the values {1,2}.
Curvilinear coordinates and local bases are extremely useful to describe free-form geometries, in particular surfaces. Two important bases are the covariant basis g_i and the contravariant basis g^i. Using them, the position vector x can be expressed as:

$$x = \theta^i g_i = \theta_i g^i \tag{4.4}$$

with θ^i and θ_i being the corresponding contravariant and covariant coordinates, respectively.
The covariant base vectors are defined as:

$$g_i = \frac{\partial x}{\partial \theta_i} = x_{,i} \tag{4.5}$$

Covariant and contravariant base vectors are related by the following condition:

$$g_i \cdot g^i = \delta_i^j = \begin{cases} 0 & \text{if } i \neq j \\ 1 & \text{if } i = j \end{cases} \tag{4.6}$$

A surface is a parametric, two-dimensional geometry: each point on the surface is described by two curvilinear coordinates, (θ^1, θ^2). Therefore, the first two covariant base vectors g_α can be computed via equation (4.5), whereas the third covariant base vector g_3 is defined as the normalized vector orthogonal to g_1 and g_2:

$$g_3 = \frac{g_1 \times g_2}{|g_1 \times g_2|} \tag{4.7}$$

The contravariant base vectors g^α lie in the tangential plane spanned by the covariant base vectors g_α, as stated by equation 4.6. Therefore, the third contravariant base vector g^3 is equal to g_3:

$$g^3 = g_3 \tag{4.8}$$

To describe surfaces, another important quantity needs to be introduced, the metric tensor g, also called identity tensor. It is expressed in the covariant and contravariant basis as:

$$g = g^{\alpha\beta} g_\alpha \otimes g_\beta = g_{\alpha\beta} g^\alpha \otimes g^\beta \tag{4.9}$$

$g_{\alpha\beta}$ represent the covariant metric coefficients and they can be computed by the scalar product between covariant base vectors:

$$g_{\alpha\beta} = g_\alpha \cdot g_\beta \tag{4.10}$$

Equation (1.8) is called the *first fundamental form of surfaces*. It is useful to get important properties of the surface, e.g. length of the base vectors and angles between them.
The contravariant metric coefficients $g^{\alpha\beta}$ are obtained by the inverse of the covariant coefficient matrix:

$$[g^{\alpha\beta}] = [g_{\alpha\beta}]^{-1} \tag{4.11}$$

The contravariant base vectors can be computed from the covariant base vectors and the contravariant metric coefficient matrix $g^{\alpha\beta}$:

$$g^\alpha = g^{\alpha\beta} g_\beta \tag{4.12}$$

Vice versa, the covariant base vectors can be computed from the contravariant base vectors and the covariant metric coefficient matrix $g_{\alpha\beta}$:

$$g_\alpha = g_{\alpha\beta} g^\beta \tag{4.13}$$

The curvature properties of a surface can be described by the *second fundamental form of surfaces*:

$$b_{\alpha\beta} = -g_\alpha \cdot g_{3,\beta} = -g_\beta \cdot g_{3,\alpha} = g_{\alpha,\beta} \cdot g_3 \tag{4.14}$$

4.3.2 Geometry of Normal Contact

Consider two deformable bodies undergoing finite deformations: according to the most common approach to contact analysis, one of them is denoted as the *slave* body $\mathrm{B^s}$ and the other one as the *master* body $\mathrm{B^m}$. This classical choice introduces a bias between the two surfaces coming into contact. The superscript i = *(s,m)* refers to the slave and master bodies, respectively, whereas d_s denotes the spatial dimension and d_p the parametric one.

The position of a generic material point in the body i in the *reference* configuration is denoted by $\mathrm{X^i}$ and the deformation of such body is expressed by:

$$x^\mathrm{i} = X^\mathrm{i} + u^\mathrm{i} \tag{4.15}$$

where **x** are the coordinates of the generic material point in the *current* configuration, and u its displacement.
The master surface is parametrized via the convective coordinates $\xi_m = \{\xi_m^\alpha\}_{\alpha=1}^{d_s-1}$; they are chosen coincident with the parametric coordinates of the surface. This means that the covariant base vectors τ_α can be computed as in equation (4.5):

$$\tau_\alpha = x^m_{,\alpha} \tag{4.16}$$

whereas the contravariant base vectors τ^α can be induced using the inverse components of the metric tensor $m_{\alpha\beta}$, as in equation (4.12):

$$\tau^\alpha = m^{\alpha\beta} \tau_\beta \tag{4.17}$$

If, during deformation, the two aforementioned bodies engage a contact, this means that the contact interface γ_c is detected.
In order to determine the unknown γ_c in the current configuration, the following distance function needs to be introduced and minimized with respect to the convective coordinates ξ_m:

$$d = \|x^s - x^m(\xi_m)\| \tag{4.18}$$

where x^s is a *fixed* point on the contact boundary γ_c^s of the slave surface and $x^m = x^m(\xi_m)$ an *arbitrary* point on the contact boundary γ_c^s of the master surface.
The solution of this minimization problem is computed under the *assumption of perfect contact*:

$$\gamma_c = \gamma_c^s = \gamma_c^m \tag{4.19}$$

This minimizer, represents the *closest projection point* of x^s on γ_c^m, i.e. the unique contact partner $\bar{x}^m = x^m(\bar{\xi}_m)$ of x^s on γ_c^m. In particular, *each point* of the slave surface needs to be projected onto the master one and *each projection* is then carried out by minimizing the distance function d, expressed in equation (4.18), as follow:

$$\frac{\partial}{\partial \xi^\alpha} d(\xi_m^1, \xi_m^2) = \frac{x^s - \bar{x}^m(\xi_m^1, \xi_m^2)}{\|x^s - \hat{x}^m(\xi_m^1, \xi_m^2)\|} \cdot \hat{x}_\alpha^m(\xi_m^1, \xi_m^2) = 0 \tag{4.20}$$

The solution of equation (4.20), requires orthogonality between the first and second term; the first term represents the conjunction between the point on the slave and the point on the master surface, while the second term, $\hat{x}_\alpha^m(\xi_m^1, \xi_m^2)$, the tangent vector.
The residual of this closest-point projection is defined as:

$$f_\alpha(\xi_m) = \tau_\alpha(\xi_m) \cdot [x^s - x^m(\xi_m)] \tag{4.21}$$

and it vanishes at the closest projection point, therefore $f_\alpha(\bar{\xi}_m) = 0$ for $\alpha = 1...(d_s - 1)$.
The search of the solution is an *iterative process*, computed by means of a Newton-Raphson scheme; it starts from an *initial guess* of parametric coordinates $\widehat{\xi_m}$ and requires the following tangent matrix to be calculated:

$$K_{\alpha\beta} = f_{\alpha,\xi_m} = x^m_{,\alpha\beta} \cdot [x^s - x^m(\xi_m)] - m_{\alpha\beta}(\xi_m) \tag{4.22}$$

The last statement must be discussed further, because finding a solution to the contact problem between two hyperelastic deformable bodies, is a nonlinear problem. In continuum mechanics, these are always solved by first linearizing the nonlinear equations and then iteratively solving the resulting linear equations, until a solution to the nonlinear problem is found. This is what the Newton-Raphson method is used for and it is the most popular example of such a technique. Only the correct linearization of the nonlinear equations leads to the right solution.
The contact interface is pulled back to $\Gamma_c := \Gamma_c^s \neq \Gamma_c^m$, where Γ_c^i is the contact boundary of body B^i in the *reference* configuration. The pull-back operation is useful to calculate all contact integrals on Γ_c^s, to facilitate the operations of linearization that will be depicted in the next subsection.

4.3.3 Variations and linearizations of the contact variables

Variations and linearizations of all the geometrical contact variables are needed in the weak form of the contact equations. From them, the linear system to be used within the Newton-Raphson scheme in order to retrieve the problem solution, can be obtained. The first variation to be computed is the variation of the normal gap (the same as in (4.1)), between the two aforesaid bodies:

$$g_N = (x^s - x^m) \cdot n \tag{4.23}$$

where n is the outward normal unit vector to the master surface at x^m,

$$n = n^m \tag{4.24}$$

As can be deduced from equation (4.23) together with the definition of n^m, g_N allows the characterization of the relative position of the two surfaces:

$$\begin{aligned} &g_N > 0 \quad \text{if } (x^s - x^m) \cdot n > 0 \rightarrow \text{contact is open} \\ &g_N < 0 \quad \text{if } (x^s - x^m) \cdot n < 0 \rightarrow \text{compenetration occurs} \\ &g_N = 0 \quad \text{if } (x^s - x^m) \cdot n = 0 \rightarrow \text{over the contact surface} \end{aligned} \tag{4.25}$$

As mentioned before, in this thesis, the *penalty method* is adopted and used to regularized the following Kuhn-Tucker conditions for impenetrability. They have to be impose on Γ_c and they state:

$$g_N \geq 0,\ t_N \leq 0,\ g_N t_N = 0 \tag{4.26}$$

In equation (4.26), t_N represents the normal contact traction vector, defined as the normal component of the Piola traction vector $t = t^m = -t^s$, where:

$$t = t_N n,\ t_N = t \cdot n \tag{4.27}$$

The result of the regularization of the contact constraints shown in equation (4.26) is:

$$t_N = \epsilon_N \langle g_N \rangle_-,\ \langle g_N \rangle_- = \begin{cases} g_N & \text{if } g_N \leq 0 \\ 0 & \text{otherwise} \end{cases} \tag{4.28}$$

Therefore, only when penetration occurs, namely when $g_N \leq 0$, the normal contact traction vector t_N exists, whereas $\epsilon_N > 0$ is the normal penalty parameter.

To compute the variation of the gap function g_N in equation (4.23), all terms which depend upon deformation have to be considered.
Consequently, recalling that $x^m = x^m(\xi_m)$ and that $\xi_m = \{\xi_m^\alpha\}_{\alpha=1}^{d_s-1}$ also relies on deformation, ∂g_N leads to:

$$\partial g_N = [\partial x^s - \partial x^m - x^m_{,\alpha} \partial \xi^\alpha] \cdot n_m + [x^s - x^m] \cdot \partial n_m \tag{4.29}$$

Equation (4.29) simplifies due to the fact that:

$$x^m_{,\alpha} \cdot n_m = 0. \tag{4.30}$$

The condition expressed by equation (4.30) has a deep meaning, i.e. the current master point is the *orthogonal* projection of a given slave point x^s onto the current master surface. Only in this case, the difference function d defined by equation (4.18) can be minimized as in (4.20).
Moreover, since the outward unit normal on the master surface at the master point $x_m\{\xi_m\}$ can also be defined as:

$$n_m = -\frac{x^s - x^m(\xi_m)}{\|x^s - x^m(\xi_m)\|} \tag{4.31}$$

this eliminates the last term in (4.29). Hence this result is obtained:

$$\partial g_N = [\partial x^s - \partial x^m] \cdot n_m. \tag{4.32}$$

In the next equations, the closest projection point and the related variables are identified with the $(\bar{\cdot})$ notation and $\bar{\eta}^\alpha$ accounts for δx^α. The linearization of the variation of the normal gap $\Delta(\delta g_N)$ is:

$$\Delta(\delta g_N) = -(\delta \bar{x}^m_{,\alpha} \Delta \xi^\alpha_m + \Delta \bar{x}^m_{,\alpha} \delta \xi^\alpha_m) \cdot \bar{n} - \delta \xi^\alpha_m k_{\alpha\beta} \Delta \xi^\beta_m + g_N \delta \bar{n} \cdot \Delta \bar{n} \tag{4.33}$$

Equation (4.33) is computed by first calculating the linearization of each term in:

$$\delta x^s - \delta \bar{x}^m - \bar{x}^m_{,\alpha} \delta \xi^\alpha = \delta g_N \bar{n}^m + g_N \delta \bar{n}^m. \tag{4.34}$$

In particular, this leads to:

$$\Delta(\delta g_N)\bar{n}_m + \delta g_N \Delta\bar{n}_m + \Delta g_N \delta\bar{n}_m + g_N \Delta(\delta\bar{n}_m) = -\Delta\bar{x}^m_{,\alpha} - \Delta\bar{x}^m_{,\alpha}\delta\xi^\alpha_m - \bar{x}^m_{,\alpha}\Delta\delta\xi^\alpha_m \tag{4.35}$$

where $\Delta(\delta x_s) = 0$.
Since x_m is a function of ξ_m which again depends on the displacement field, the second member of equation (1.31) reduces to:

$$\Delta(\delta g_N)\bar{n}_m + \delta g_N \Delta\bar{n}_m + \Delta g_N \delta\bar{n}_m + g_N \Delta(\delta\bar{n}_m) = -[\bar{\eta}^m_{,\alpha}\Delta\xi^\alpha + \Delta\bar{u}^m_{,\alpha}\delta\xi^\alpha + \bar{x}^m_{,\alpha\beta}\Delta\xi^\beta\delta\xi^\alpha + \bar{x}^m_{,\alpha}\Delta\delta\xi^\alpha] \tag{4.36}$$

where Δu^γ are the increments of $x^\gamma = X^\gamma + u^\gamma$ and $\Delta\xi^\alpha$ denotes the increment of ξ^α. Note that in equation (4.36) $\Delta\xi^\alpha$, $\delta\xi^\alpha$, $\Delta\delta\xi^\alpha$, $\Delta\bar{n}^m$, $\delta\bar{n}^m$ and $\Delta\delta\bar{n}^m$ are still unknown. By multiplication of both members with $\bar{n}_m$, equation (1.32) can be solved for $\Delta(\delta g_N)$:

$$\Delta(\delta g_N) = -[\bar{\eta}^m_{,\alpha}\Delta\xi^\alpha + \Delta\bar{u}^m_{,\alpha}\delta\xi^\alpha + \bar{x}^m_{,\alpha\beta}\Delta\xi^\beta\delta\xi^\alpha] - g_N\bar{n}^m \cdot \Delta\delta\bar{n}^m. \tag{4.37}$$

Note that a lot of terms disappeared due to the following identities:

$$\begin{aligned} \bar{n}_m \cdot \delta\bar{n}_m &= 0 \\ \bar{n}_m \cdot \bar{x}^m_{,\alpha} &= 0. \end{aligned} \tag{4.38}$$

At this point, the only unknown term is $\bar{n}_m \cdot \Delta\delta\bar{n}_m$. It can be rewritten as:

$$\Delta(\bar{n}_m \cdot \delta\bar{n}_m) = \Delta\bar{n}_m \cdot \delta\bar{n}_m + \bar{n}_m \cdot \Delta\delta\bar{n}^m = 0. \tag{4.39}$$

From this identity, the last term follows as:

$$-g_N\bar{n}^m \cdot \Delta\delta\bar{n}^m = g_N\Delta\bar{n}^m \cdot \delta\bar{n}^m. \tag{4.40}$$

The variation and linearization of the normal at the projection point has now to be computed. Since the orthogonality condition $\bar{n}_m \cdot \bar{x}^m_{,\alpha} = 0$ between the normal and the tangent vector at the projection point holds, its variation can be computed and reads as follows:

$$\delta\bar{n}_m \cdot \bar{x}^m_{,\alpha} = -\bar{n}_m \cdot \delta\bar{x}^m_{,\alpha}. \tag{4.41}$$

Recalling the definition of tensor product between vectors,

$$(u \otimes v)w = (w \cdot v)u \tag{4.42}$$

equation (4.41) can be solved for the variation of the normal vector:

$$\delta\bar{n}_m = -(\bar{n}_m \cdot \delta\bar{x}^m_{,\alpha})\bar{x}^{m,\alpha} = -[\bar{x}^{m,\alpha} \otimes \bar{n}_m]\delta\bar{x}^m_{,\alpha} \tag{4.43}$$

where $\bar{x}^m_{,\alpha} = [\bar{x}^{m,\alpha}]^{-1}$ and vice versa. Expressing the contravariant base vector by the covariant tangent vector as:

$$\bar{x}^{m,\alpha} = \bar{x}^{,\alpha\beta}\bar{x}^m_{,\beta} \tag{4.44}$$

equation (4.43) results in:

$$\delta\bar{n}_m = -(\bar{n}_m \cdot \delta\bar{x}^m_{,\alpha})\bar{x}^{,\alpha\beta}\bar{x}^m_{,\beta}. \tag{4.45}$$

In the same way the linearization of the normal vector is derived as:

$$\Delta\bar{n}_m = -(\bar{n}_m \cdot \Delta\bar{x}^m_{,\alpha})\bar{x}^{m,\alpha} = -[\bar{x}^{m,\alpha} \otimes \bar{n}_m]\Delta\bar{x}^m_{,\alpha} = -(\bar{n}_m \cdot \Delta\bar{x}^m_{,\alpha})\bar{x}^{,\alpha\beta}\bar{x}^m_{,\beta}. \tag{4.46}$$

The variation and linearization of the base vector $\bar{x}^m_{,\alpha}$ are given by:

$$\delta\bar{x}^m_{,\alpha} = \delta\bar{u}^m_{,\alpha} + \bar{x}^{,\alpha\beta}\delta\xi^\beta \quad \text{and} \quad \Delta\bar{x}^m_{,\alpha} = \Delta\bar{u}^m_{,\alpha} + \bar{x}^{,\alpha\beta}\Delta\xi^\beta \tag{4.47}$$

Once the linearization of the base vectors $\delta\bar{x}^m_{,\alpha}$ is expressed by the incremental displacements, the linearization of the normal vector is completed.
By insertion of the obtained results into equation (4.37), the final result can be given after some algebraic manipulations:

$$\Delta(\delta g_N) = -[\bar{\eta}^m_{,\alpha}\Delta\xi^\alpha + \Delta\bar{u}^m_{,\alpha}\delta\xi^\alpha + \bar{x}^m_{,\alpha\beta}\Delta\xi^\beta\delta\xi^\alpha]\cdot\bar{n}^m + g_N\bar{n}^m\cdot(\bar{\eta}^m_{,\alpha} + \bar{x}^{,\alpha\beta}\delta\xi^\beta)\bar{x}^{,\alpha\gamma}(\Delta\bar{u}^m_{,\gamma} + \bar{x}^{,\gamma\theta}\Delta\xi^\theta)\cdot\bar{n}^m. \tag{4.48}$$

$\Delta(\delta g_N)$ is symmetric with respect to variation and linearization: consequently, its contribution to the contact stiffness matrix within the NURBS-based discretization, is also symmetric.

always symmetric in variation and linearization. Equation (4.48) is equal to (4.33), after substitution of all the quantities computed so far and expressing the dependency from the displacement field.

4.3.4 Contact virtual work

The frictionless contact problem between two deformable hyperelastic bodies, already introduced in (4.2), can be formulated as the *constrained minimization* of the potential energy function W. The constraints are the Khun-Tucker conditions for impenetrability, shown in (1.23), and regularized with a penalty solution method (equation (1.25)). The variation of the contact virtual work is:

$$\delta\Pi_c = \int_{\Gamma_c} t_N\delta g_N d\Gamma = \epsilon_N\int_{\Gamma_C} g_N\delta g_N d\Gamma \tag{4.49}$$

Its linearization yields:

$$\Delta\delta\Pi_c = \epsilon_N\int_{\Gamma_C}\Delta g_N\delta g_N d\Gamma + \epsilon_N\int_{\Gamma_C} g_N\Delta(\delta g_N)d\Gamma \tag{4.50}$$

From equation (4.50), the consistent tangent stiffness matrix K_T, shown in equation (4.22), can be computed.
Thus, introducing NURBS interpolations into (4.32) and (4.33), considering also that the linearization of Δg_N has the same structure as the variation of g_N, shown in (4.32):

$$\Delta g_N = [\Delta x^s - \Delta x^m]\cdot n_m \tag{4.51}$$

their respective matrix form $\delta g_N = \delta u^T N,\ \Delta g_N = N^T\Delta u$ can be obtained, upon definition of the following vectors:

$$\delta u = \begin{bmatrix}\delta u^s_1\\ \vdots\\ \delta u^s_{n^s}\\ \delta u^m_1\\ \vdots\\ \delta u^m_{n^m}\end{bmatrix},\quad \Delta u = \begin{bmatrix}\Delta u^s_1\\ \vdots\\ \Delta u^s_{n^s}\\ \Delta u^m_1\\ \vdots\\ \Delta u^m_{n^m}\end{bmatrix},\quad N = \begin{bmatrix}R^s_1(\xi_s)n\\ \vdots\\ R^s_{n^s}(\xi_s)n\\ -R^m_1(\xi_m)n\\ \vdots\\ -R^m_{n^m}(\xi_m)n\end{bmatrix} \tag{4.52}$$

where $\xi_s = \{\xi^\alpha_s\}^{d_s-1}_{\alpha=1}$ are the parametric coordinates of the point on the slave surface where quantities are currently being evaluated and $\xi_m = \{\xi^\alpha_m\}^{d_s-1}_{\alpha=1}$ are the parametric coordinates of the respective projection point on the master surface.
In this thesis, the contact formulation that has been employed is the one known as Gauss-point-to-surface (GPTS). The name derives from the fact that the contact contribution to the virtual work δW_c in equation (4.49), is integrated by locating a predetermined number of Gauss-Legendre quadrature points *on each element* of the slave contact surface. This also means that the integration is performed at element level.
One thing must be stressed: Gauss-Legendre quadrature performs well with polynomial basis functions. NURBS basis functions are rational polynomials and not polynomials: therefore, with NURBS, the

integration with Gauss quadrature is only approximative, even if it has been proved reliable. However, it must be reminded that not the basis function per se are integrated but the element formulation, resulting in the integration of rational polynomials anyhow.
Hence, in vector N, ξ_s refers to the parametric coordinates of the i-th Gauss point. Computation of the integral, which now reduces to a combination, through the weights w_g, of the NURBS basis function evaluated at the coordinates of each Gauss point, is combined with an *active set strategy*: the summation is extended to all the quadrature points with negative values of the gap g_N. Note that the quadratures are pre-defined on the surface.
The dimension of each vector in (4.52) is $[(n_s+n_m)\times 1]$ where n_s and n_m are the number of basis function having support on the element of the slave and master body, respectively. In case of GPTS formulation, the values of n_s and n_m don't change, because following the standard definition in isogeometric analysis, an element is defined as a tensor product domain of distinct knot intervals. In each element $(p+1)\times(q+1)$ quadratures are placed, where p and q are the degrees. But, considering NURBS, the local support of each basis function is exactly $(p+1)\times(q+1)$, and so the two concept matches.
From equation (4.33) the linearization of the variation is obtained as follows:

$$\Delta(\delta g_N) = \delta u^T k_{geo} \Delta u \tag{4.53}$$

where

$$k_{geo} = g_N \bar{N} m^{-} 1 \bar{N}^T + D\hat{N}^T + \hat{N}D^T - DkD^T \tag{4.54}$$

In equation (4.54), m^{-1} is the inverse of the metric tensor m, the same as g in equation (4.9). Its component are $m^{\alpha\beta}$. k is the curvature tensor $k_{\alpha\beta}$ and it matches $b_{\alpha\beta}$ in (4.14).
The following quantities:

$$N_\alpha = \begin{bmatrix} 0 \\ \vdots \\ 0 \\ -R^m_{1,\alpha}(\xi_m)n \\ \vdots \\ -R^m_{n^m,\alpha}(\xi_m)n \end{bmatrix}, \quad T_\alpha = \begin{bmatrix} R^s_1(\xi_s)\tau_\alpha \\ \vdots \\ R^s_{n^s}(\xi_s)\tau_\alpha \\ -R^m_1(\xi_m)\tau_\alpha \\ \vdots \\ -R^m_{n^m}(\xi_m)\tau_\alpha \end{bmatrix} \tag{4.55}$$

leads to the definition of:

$$\hat{N} = [N_1\ N_2] \quad \hat{T} = [T_1\ T_2] \quad D = [\hat{T} - g_N\hat{N}]A^{-1} \quad \bar{N} = \hat{N} - Dk \tag{4.56}$$

where A^{-1} is deduced from the inverse of $A_{\alpha\beta} = m_{\alpha\beta} - g_N k_{\alpha\beta}$. All the previous equations are valid for both 2D and 3D cases, except for $\hat{N}$ and $\hat{T}$ that in 2D case reduce to: $\hat{N} = N_1$ and $\hat{T} = T_1$, where $\alpha = 1$, which means that the derivative is taken with respect to the first parametric coordinate. This is our case because, in this work, the parametric dimension d_s is two.

$$N_1 = \begin{bmatrix} 0 \\ \vdots \\ 0 \\ -R^m_{1,1}(\xi_m)n \\ \vdots \\ -R^m_{n^m,1}(\xi_m)n \end{bmatrix}, \quad T_1 = \begin{bmatrix} R^s_1(\xi_s)\tau_1 \\ \vdots \\ R^s_{n^s}(\xi_s)\tau_1 \\ -R^m_1(\xi_m)\tau_1 \\ \vdots \\ -R^m_{n^m}(\xi_m)\tau_1 \end{bmatrix} \tag{4.57}$$

From equation (4.50), the expression of the consistent tangent stiffness matrix can be derived:

$$K_T = K_{T,material} + K_{T,geometric} \tag{4.58}$$

In particular, in (4.50) $\epsilon_N \int_{\Gamma_C} \Delta g_N \delta g_N d\Gamma$ accounts for $K_{T,material}$, the material component of the tangent stiffness matrix, whereas $\epsilon_N \int_{\Gamma_C} g_N \Delta(\delta g_N) d\Gamma$ accounts for $K_{T,geometric}$, the geometric one. They are given by:

$$K_{T,material} = \epsilon_N \int_{\Gamma_C} N N^T d\Gamma \tag{4.59}$$

$$K_{T,geometric} = \epsilon_N \int_{\Gamma_C} g_N k_{geo} d\Gamma \tag{4.60}$$

and obtained by simply replacing in (4.50) δg_N with $\delta u^T N$, and Δg_N with $N^T \Delta u$. Their numerical integration with Gauss-Legendre quadrature, always combined with the active set strategy previously mentioned, yields:

$$K_{T,material} = \epsilon_N \sum_{GP,active} N_g N_g^T w_g j_g \tag{4.61}$$

$$K_{T,geometric} = \epsilon_N \sum_{GP,active} g_{N_g} k_{geo,g} w_g j_g \tag{4.62}$$

where w_g and j_g are the weight and the jacobian associated to the same Gauss point. The expression for *kgeo* can be found in (4.54)

The tangent stiffness matrix K_T is symmetric and it can be rewritten as:

$$\begin{array}{r|l} K_{ss} & K_{sm} \\ \hline K_{ms} & K_{mm} \end{array} \tag{4.63}$$

Each block has the following dimension:

$$\begin{aligned} &K_{ss} \rightarrow [n_s \times n_s] \\ &K_{sm} \rightarrow [n_s \times n_m] \\ &K_{ms} \rightarrow [n_m \times n_s] \\ &K_{mm} \rightarrow [n_m \times n_m] \end{aligned} \tag{4.64}$$

Once K_T has been calculated, the contact contribution to the residual vector for the Newton-Raphson iterative solution of the nonlinear problem, must be obtained as follows:

$$R = \epsilon_N \int_{\Gamma_C} g_N N d\Gamma \tag{4.65}$$

whereas its numerical computation on Γ_c leads to:

$$R = \epsilon_N \sum_{GP,active} g_N N_g w_g j_g. \tag{4.66}$$

All these quantities must be included within the Newton-Raphson scheme: its goal is minimizing the scalar product between the conjunction between $x^s(\xi)$ and $x^m(\xi)$, called $r(\xi)$, and the tangent vector $t(\xi)$ evaluated at the guess parametric coordinate; hence, all the previous equations serve to achieve this objective. The contact projection algorithm can be then summarized as follow:

4.4 NURBS 3D contact driver for FEAP

In this section, the contact driver contained within the IgA package for the general purpose solver FEAP ("Finite Element Analysis Program") is introduced. This contact driver reproduces the non-mortar KTS algorithm proposed by De Lorenzis et al. for NURBS discretizations [24] and by Dimitri et al. [10] for T-spline discretizations. Each portion of the contact driver is described in detail by means of a table, whose goal is also to link the equations described in section (4.3.2) to every block of the algorithm.
The contact model is considered frictionless, i.e., only normal contact forces are transmitted whereas the contact constraint is regularized with a penalty method.

Step 1: **SEARCH ALGORITHM**.
For each slave Gauss point on the slave surface, the contact pair is defined by the point itself and its unknown projection on the master surface. A Newton-based scheme is use to find the projection point; the search routine'main goal is finding the best initial guess for the Newton loop. In order to reduce the computational domain for the subsequent projection routine, the projection is assumed to be confined between all the elements connected to the closest master control point. In particular, the following information are stored for domain reduction:

- For each slave Gauss point $x_s(\xi)$, the parametric coordinates of the closest control point on the master surface;
- All the information related to the facets connected with the closest control points.

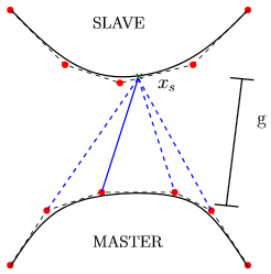	Search routine aims at finding the best initial guess for the Newton loop.

Table 4.2: Search algorithm: Gauss points on the slave surface are identified with x. The initial contact pair guess, prior to projection, is highlighted by the full blue line [14].

Step 2: **PROJECTION**.
For each slave Gauss point $x_s(\xi)$ the closest point projection $x_m(\xi)$ on the master surface is retrieved by means of a Newton-based scheme that minimizes the scalar product between the conjunction between $x_s(\xi)$ and $x_m(\xi)$, called $r(\xi)$ and the tangent vector $t(\xi)$ evaluated at the guess parametric coordinate. For the sake of clarity, the projection algorithm is summarized in Box 1.

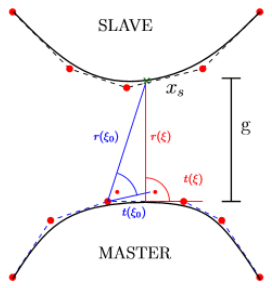	Equations involved in projection step: from (**4.18**) to (**4.20**).	For each slave Gauss point $x_s(\xi)$ the closest point projection $x_m(\xi)$ on the master surface is determined.

Table 4.3: Projection algorithm: initial (guess) and final projections are defined in blue and red, respectively [14].

The following information are required and stored in this step:

- Given an initial guess, all the information regarding the facets connected with this initial guess are obtained in order to improve projection. In case of projection failure in a facet, the algorithm automatically switches to the other stored facets.
- The solution ξ at the i^{th} Newton loop is saved and used as initial guess for the subsequent Newton step.

BOX 1: CONTACT PROJECTION ALGORITHM

SET INITIAL GUESS ξ (SEARCH)

LOOP OVER MAX NUMBER OF ITERATIONS
EVALUATE $\mathbf{x}_m(\xi)$
COMPUTE $\mathbf{r}(\xi)$=$\mathbf{x}^m(\xi)$-$\mathbf{x}^s(\xi)$ and the Jacobian $\mathbf{J}(\mathbf{r})$
COMPUTE $f(\xi)$=$\mathbf{r}(\xi) \cdot \mathbf{t}(\xi)$
IF $f \leq tol$
CONVERGENCE$\longrightarrow$ STORE PAIR INFORMATION
BREAK
ELSE
$d\xi$=-$f(\xi)/J(\mathbf{r})$
ξ=ξ+$d\xi$
NEXT

Step 3/4/5: **RESIDUAL**, **STIFFNESS** and **ASSEMBLY** routines.
Once having all the information about contact pair, stiffness and residual contributions are computed by following the standard structure of penalty-based frictionless contact formulation [10] and assembled into the global data structure. Stiffness and residual contributions are calculated at active gauss point level (i.e., gauss point that are effectively in contact) and then assembled at degree of freedom level.

Main goal	Equation labels
Calculation of all the quantities required for the residual and stiffness routines at parametric dimension and gauss point level.	Eq. from (**4.52**) to (**4.55**).
Calculation of the residual vector at active gauss point level.	Eq. (**4.66**).
Computation of the stiffness matrices at active gauss point level.	• Material stiffness matrix: Eq.(**4.61**); • Geometric stiffness matrix: Eq.(**4.62**); • Overall stiffness matrix: Eq.(**4.58**).

Table 4.4: Equations involved in Residual and Stiffness routines.

4.5 Shell Normal Contact

Shell normal contact is based on the previous equations. One thing must be stressed: the contact discretized surface is a *bivariate* NURBS that is directly inherited from the *bivariate* NURBS shell spatial discretization (this means that only two knot vectors must be introduced). This is not a mistake: even though it is an element which develops in the three dimensional space, shell continuum is discretized using a bivariate NURBS; shell thickness comes directly from the element formulation. Moreover, in this work, the shell middle surface has been taken as reference, i.e. knot vector together with the associated control points and the accompanying weights refer to the surface associated with thickness equals to zero. This is a plausible choice because the element that has been used within this work is the thin shell element based on the Kirchoff-Love shell theory. Therefore, according to it, transverse shear deformation is neglected and the director, i.e. the vector normal to the middle surface, remains normal in the deformed configuration. The description of the shell can then be reduced to the description of its middle surface.

Chapter 5

Numerical Results

The KTS IgA contact driver presented in Chapter 4 has been implemented in the finite element code FEAP. Some numerical examples have been solved in order to demonstrate its projection capability in combination with NURBS discretizations. More specifically, KTS contact driver was tested by means of three numerical tests, characterized by increasing complexity. The NURBS-based geometries depicted in the following pictures are created and refined by means of GeoPDEs software, a suite of tools for research on Isogeometric Analysis of PDEs [5]. For each test, the penalty parameter for which the most accurate results are obtained is given. Its value was tuned in order to assess the effect on results. The following trend applied to all the tests performed: lower penalty values leads to a poor match between numerical results. This effect is due to the large penetrations affecting the penalty solution.
A remark must be done: the following tests are preliminary and are proposed with the only scope of testing and comparing the considered formulations on some classical benchmark problems, rather than performing simulations of actual physical problems, which will be the object of future developments. Accordingly, applied forces, displacements, boundary conditions, and material properties do not represent physically or clinically relevant quantities.
It is also highlighted that, in Chapter 3, Kirchhoff-Love shell elements have been introduced and discussed, but no numerical tests involving them are herein presented, since the complete implementation and testing of their behavior in the context of contact problems is still a work in progress.

5.1 Materials and Methods

In this section the computational framework to obtain IgA-suitable models is described. Subsequently, the constitutive model used in the study is described. In particular, a formulation under the hypothesis of large displacements and large strains is adopted. Such geometrical models and constitutive laws are then integrated within a displacement analysis setup.

5.1.1 Geometry modeling

The NURBS surface for each of the three tests is created and extruded by means of a in-house MATLAB code (The Mathworks Inc. Natick, MA, USA), leading to the final geometry. The trivariate NURBS structure is then exported in a suitable format for the software FEAP. A tie process is performed in order to connect separate parts of the mesh (where needed). Given the basic NURBS representation, the refinement techniques that are adopted for IgA and FEA are respectively:

- For the IgA models a k-refinement routine is used. K-refinement was introduced in Chapter 2. This approach allows to elevate the polynomial order and, at the same time, to increase the smoothness of the basis function. Starting from the IgA basic model, the IgA k-refinement steps are:

  1. Degree elevation;
  2. Knot insertion.

The previous steps must be followed in the given order. For the sake of simplicity, Table (5.1.1) aims at better explaining how IgA k-refinement works.

IgA k-refinement		
IgA basic model	ξ={0 0 0 0.25 0.25 0.5 0.5 0.75 0.75 1 1 1} η = {0 0 1 1}	Num. of Control Points = 18
Degree Elevation	ξ={0 0 0 0.25 0.25 0.5 0.5 0.75 0.75 1 1 1} η = {0 0 0 1 1 1}	Num. of Control Points = 27
Knot Insertion	ξ={0 0 0 0.25 0.25 0.5 0.5 0.75 0.75 1 1 1} η = {0 0 0 0.5 1 1 1}	Num. of Control Points = 39

- In order to obtain a set of reliable finite element meshes in a straightforward way directly from a NURBS model of order p, the refinement that has been used firstly perform a series of knot insertions and then the obtained p-high-order refined model is transformed into a linear low-order one, so that the continuity between elements is the classical FEA C^0 continuity whereas the connectivity between them is directly inherited from the NURBS high-order model.

5.1.2 Constitutive Model

The analysis are performed by using an isotropic hyperelastic Neo-Hookean material model. It is deduced from the following strain energy function:

$$W = (K - \frac{2}{3}G)U(J) + \frac{1}{2}G(I_C - 3 - 2ln(J)) \tag{5.1}$$

Strain energy function in equation (3.12) is expressed in terms of the invariants of the deformation tensor C. In particular,

$$I_C = tr(C) \tag{5.2}$$

Being J the determinant of the deformation gradient F, the function U(J) is defined in FEAP as:

$$U(J) = \frac{1}{4}(J^2 - 1 - 2ln(J)) \tag{5.3}$$

In equation (5.1) the perameters K and G are equivalent to the small strain bulk and shear moduli, respectively. Input data for the model is specified in terms of the equivalent small strain modulus E and Poisson ration ν, such that K and G are given by:

$$K = \frac{E}{3(1-2\nu)} \tag{5.4}$$

$$G = \frac{E}{3(1+\nu)} \tag{5.5}$$

For each test, the related material properties are specified.

5.2 Analysis Setup

The goal is to evaluate the potential of IgA in simulating contact phenomena comparing its performance with respect to classical FEA. Therefore, in order to evaluate the suitability of the given approach, the convergence of IgA and FEA is tested by considering stored energy as a global reference quantity for the assessment with respect to the number of DOF. All the subsequent analysis are performed with FEAP and 1 CPU. Three test will be shown in the following sections. They are characterized by increasing difficulty in determining the outward normal evaluated at the projection point. This is particularly evident in case of curve and coarse meshes. Table (5.1) gives a hint of the geometries that are investigated. For each of them, a table is also provided in order to summarize the performance in terms of average number of steps and minimum and maximum values of the gap for the contact pair

for a given penalty parameter. The value of the gap that is considered is the one relative to the last time step and to the images shown in the following tables.

TEST	GEOMETRY CHARACTERISTICS
Plate (Master) - Emicylinder (Slave)	A curve surface is projected into a plane one.
Plate (Slave) - Cylinder (Master)	A plane surface is projected into a curved one.
Cylinder (Slave) - Cylinder (Master)	A curved surface is projected into a curved one.

Table 5.1: Summary of the performed tests.

5.3 Results

5.3.1 Plate - Emicyilinder test

In the so called Rigid Plate - Emicylinder contact test, a slave deformable emicylinder body comes in contact with a rigid master plate by means of a displacement-controlled analysis. The search of the projection onto the master surface is straightforward, since the master geometry is plane and therefore no problems in defining the normal vector evaluated at each projection point should be found. The problem is solved with a globally refined NURBS mesh with uniform knot vectors and the same order of parametrization (i.e., p = 3). A Neo-Hookean material law is adopted for both bodies with constant parameters E=5 GPa and $\nu = 0.3$.
The lower body, the plate, is completely rigid, whereas the emicylinder is constrained as shown in Table (5.2). A uniform vertical displacement $U_z = -1.2$ mm is applied to the slave nodes in 10 time steps. The penalty parameter is $\epsilon_N = 1e^8$. Results are depicted in Table (5.4) in terms of displacement along x, y and z axes and Von Mises stress.

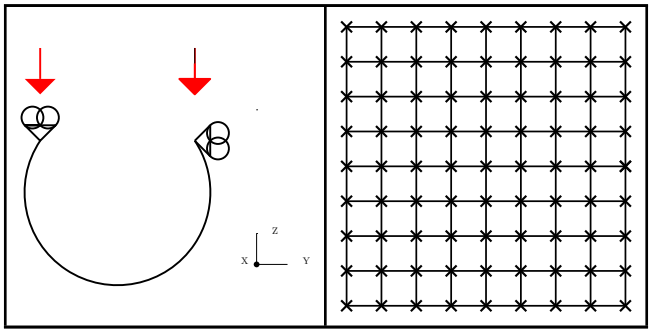

Table 5.2: Boundary condition summary for the plate-emycilinder test. The red arrows depicted in the figure on the left, represents the uniform vertical displacement $U_z = -1.2$ mm imposed on emicylinder upper nodes. Black crosses in the figure on the right means that all the nodes of the plate are fixed on x, y and z direction.

In order to evaluate the effect of refinement on strain energy, given the refinement techniques for IgA and FEA presented in section (5.1.1), different IgA and FEA NURBS-meshes are constructed for a default value of the penalty parameter (i.e. $\epsilon_N = 1e^8$). In particular, 5 k-refined IgA meshes and 5 refined FEA meshes are created, namely "IGA2", "IGA5", "IGA7", "IGA10", "IGA20" for the IgA and "FEA2", "FEA5", "FEA7", "FEA10", "FEA20" for the FEA. The number after the name "IGA" or "FEA" is relative to the number required by the in-house Matlab code to perform knot insertion operations. Higher is its value, more refined is the mesh. Table (5.3) lists the number of DOF per mesh. By refining the mesh, the number of Gauss points where the contact constraints are enforced is also varied. An increasing number of Gauss points is beneficial, as it improves the resolution in the

computation of contact strain energy, the global quantity chosen for the evaluation (see Figure 5.1 and 5.2). The images presented in Tables (5.4) and (5.6) are relative to models "IGA10" and "FEA10", respectively.

IGA MESH NAME	FEA DOF	FEA MESH NAME	IGA DOF
IGA2	81	FEA2	148
IGA5	954	FEA5	1589
IGA7	2456	FEA7	3591
IGA10	6828	FEA10	28716
IGA20	51219	FEA20	63886

Table 5.3: Number of DOF of the constructed FEA and IgA meshes.

5.3.2 Plate - Emicylinder Test: IgA results

In Table (5.4) the results for the IgA-based plate-emicylinder test are shown.

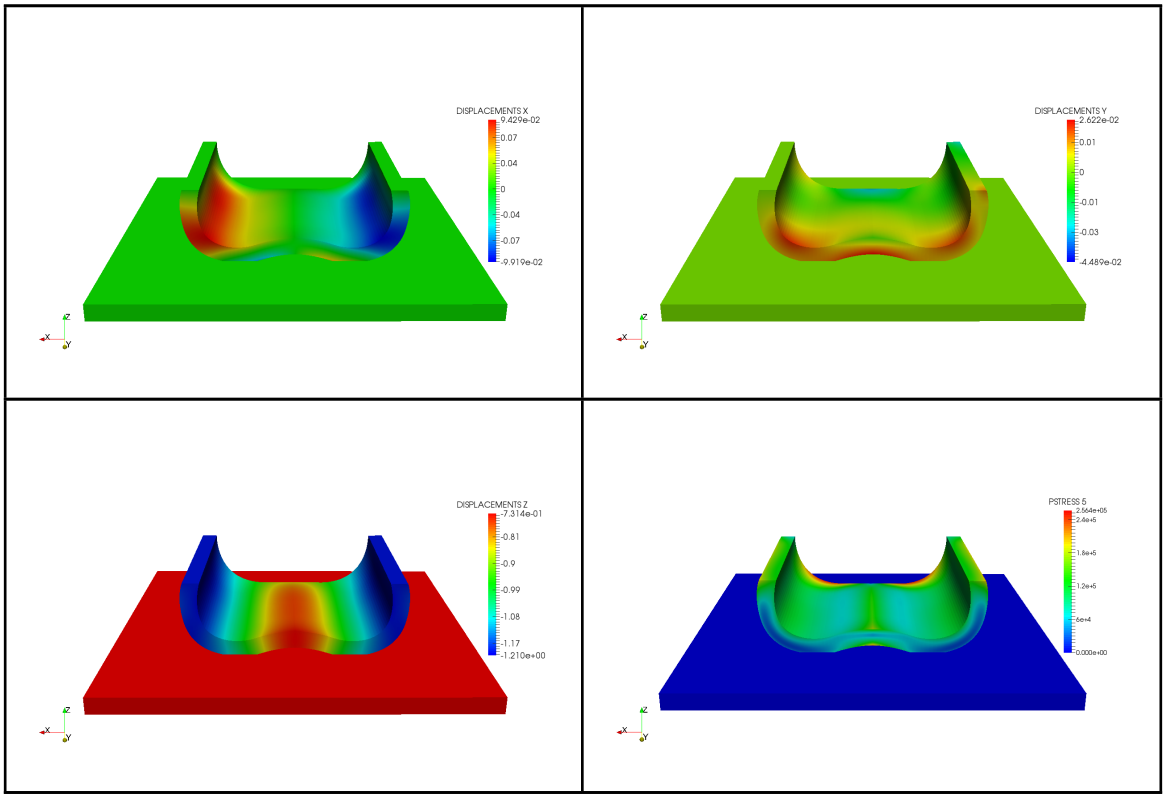

Table 5.4: Deformed IgA shapes, displacements and Von Mises stress contours for time step 10.

Avg iteration Number/Step	5
Gap Minimum at last time step	-6.5408e-04 mm
Gap Maximum at last time step	7.2439e-01 mm
CPU Time	143.91 sec

Table 5.5: Summary of the tests performed in terms of average iteration number/step for the mesh in table 5.4 for the given penalty parameter $\epsilon_N = 1e^8$.

5.3.3 Plate - Emicyilinder Test: FEA results

In Table (5.6) the results for the FEA-based plate-emicylinder test are shown.

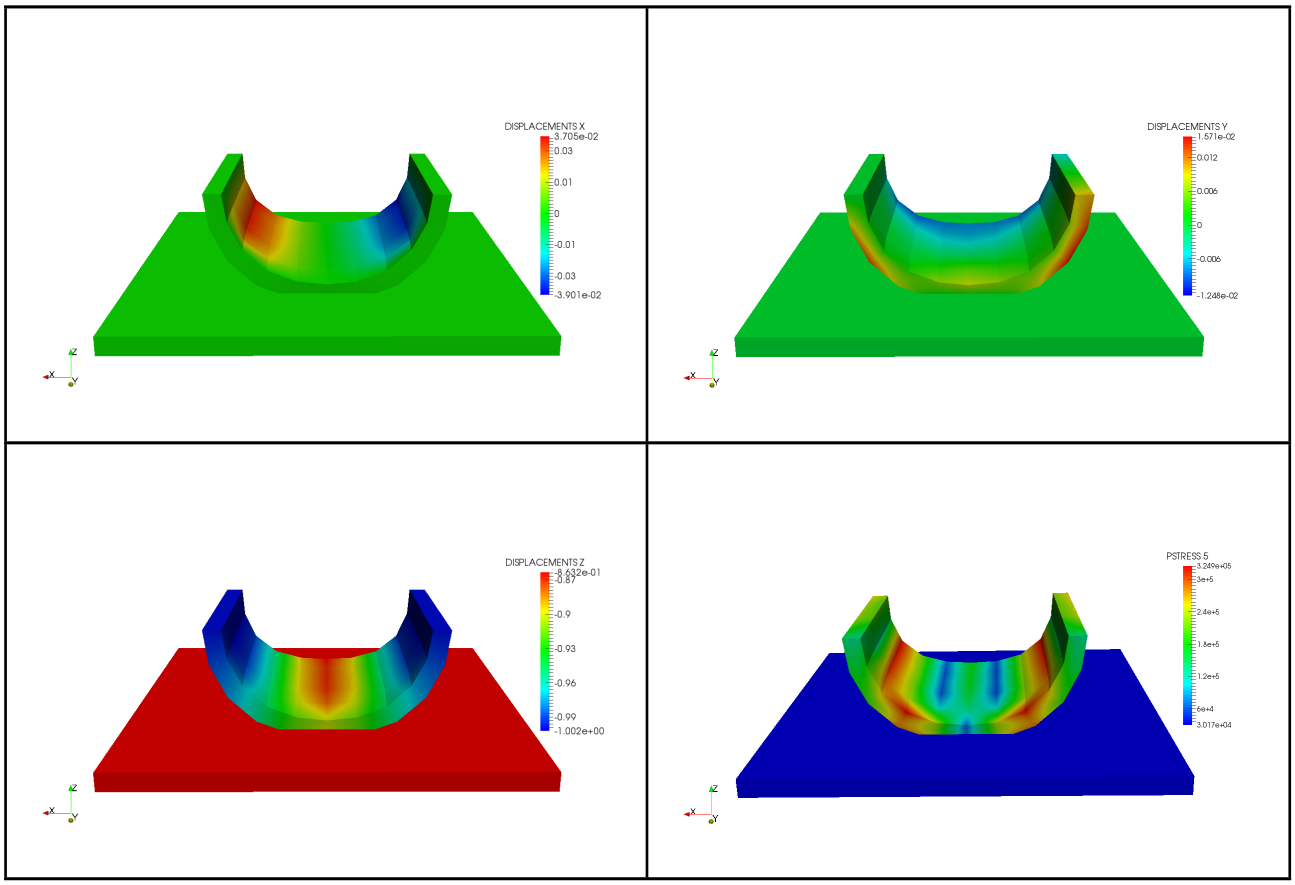

Table 5.6: Deformed FEA shapes, displacements and Von Mises stress contours for time step 10.

Avg iteration Number/Step	7
Gap Minimum at last time step	-2.2431e-03 mm
Gap Maximum at last time step	9.3467e-01 mm
CPU Time	370.57 sec

Table 5.7: Summary of the tests performed in terms of average iteration number/step for the mesh in table (5.6) for the given penalty parameter $\epsilon_N = 1e^8$.

IgA and FEA strain energy of the obtained meshes is plotted with respect to time in Figures (5.1) and (5.2) respectively.
The comparison between Figures (5.1) and (5.2) shows that, for a default value of the penalty parameter (i.e. $\epsilon_N = 10^8$), IgA strain energy values are always lower than the correspondent FEA strain energy ones. In Figure (5.3), IgA and FEA strain energy values are plotted against DOF. The results demonstrates that IgA has got a better performance with respect to FEA on a per-degree-of-freedom basis in terms of convergence. This results is qualitatively in accordance with other theoretical results [7]. Specifically, IgA converges better and faster than FEA. Moreover, by comparing Von Mises stress in the two cases, FEA Von Mises stress (see Table 5.6) oscillates. This can be seen by contrasting their contour plots. The reason is that whereas the displacement solution is similar for both IgA and FEA, Von Mises stress has several differences due to the diverse continuity between elements.

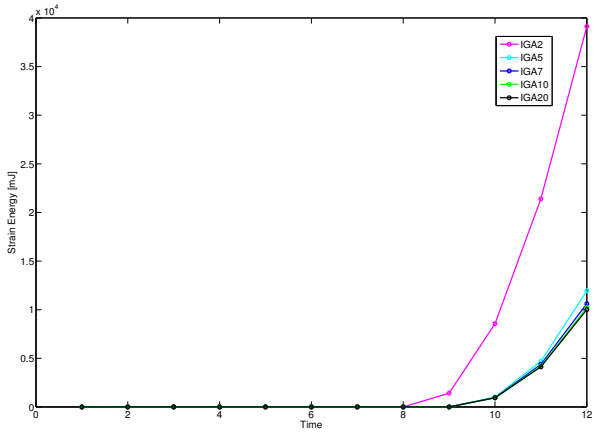

Figure 5.1: IgA strain energy vs time.

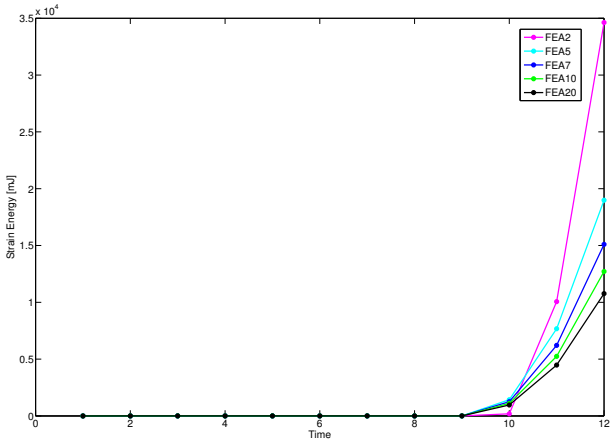

Figure 5.2: IgA strain energy vs time.

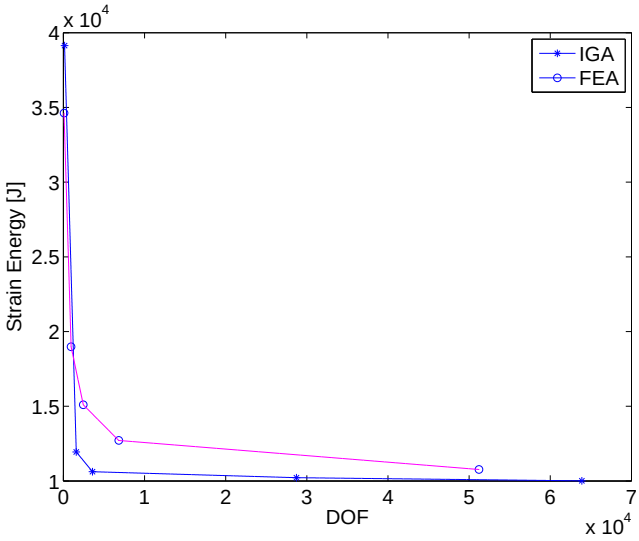

Figure 5.3: IgA and FEA strain energy vs DOF: convergence plot

5.3.4 Plate - Cylinder Test

The so called "Plate - Cylinder" test is different from the previous one because it is characterize by the need to project into a curved master surface. Therefore, the search of the projection is difficult in case of non-smooth, curved and coarse meshes. In case of curved coarse meshes, in fact, the outward normal evaluated at the projection point is not easy to be determined and oscillations in the search of the projection may occur. In this example, the cylinder (discretized with quadratic-quadratic-linear elements) is the master body, whereas the plate (quadratic-quadratic-linear elements) is the slave body. The deformable plate comes in contact with the deformable master cylinder surface by means of a displacement-controlled analysis. An hyperelastic neo-Hookean material behavior is considered for both master and slave, with constants $E = 5\text{GPa}$ and $\nu = 0.3$, whereas a uniform downward displacement $U_y = -1\text{mm}$ is applied to the upper surface of the plate in 10 time steps. The problem is solved with a globally refined NURBS mesh with uniform knot vectors. The two bodies are constrained as in Table (5.8)

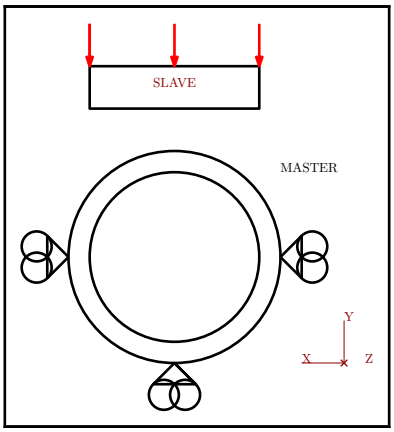

Table 5.8: Boundary condition summary for the plate-cylinder test. The red arrows represent the uniform vertical displacement $U_y = -1$ mm imposed on plate boundary nodes.

The effect of refinement has been tested also for the Plate-Cylinder case study. Specifically, given the refinement techniques for IgA and FEA presented in section (5.1.1), different IgA and FEA NURBS-meshes are constructed for a default value of the penalty parameter (i.e. $\epsilon_N = 1e^8$). In particular, 4 k-refined IgA meshes and 4 refined FEA meshes are created, namely "IGA5", "IGA7", "IGA10", "IGA20" for the IgA and "FEA5", "FEA7", "FEA10", "FEA20" for the FEA. Also in this case, the number after the name "IGA" or "FEA" is relative to the number required by the in-house Matlab code to perform knot insertion operations. The rule "higher is its value, more refined is the mesh", still holds. Table (5.9) lists the number of DOF per mesh. Results can be seen from Figure (5.10) to (5.12). The considerations made for the Plate-Emicylinder test still hold for the Plate-Cylinder one. IgA strain values, for a given value of the penalty parameters (i.e., $\epsilon_N = 1e^8$) are lower than the correspondent FEA ones. The results show that IgA again results in a better performance with respect to FEA on a per-degree-of-freedom basis, with a gain of over one order of magnitude in DOF number. The images presented in Tables (5.10) and (5.12) are relative to models "IGA10" and "FEA10", respectively.

IGA MESH NAME	FEA DOF	FEA MESH NAME	IGA DOF
IGA5	780	FEA5	1966
IGA7	2116	FEA7	3286
IGA10	2915	FEA10	5896
IGA20	11235	FEA20	20056

Table 5.9: Number of DOF of the FEA and IgA meshes respectively.

5.3.5 Plate - Cyilinder Test: IgA results

In Table (5.10) the results for the IgA-based plate-cylinder test are shown.

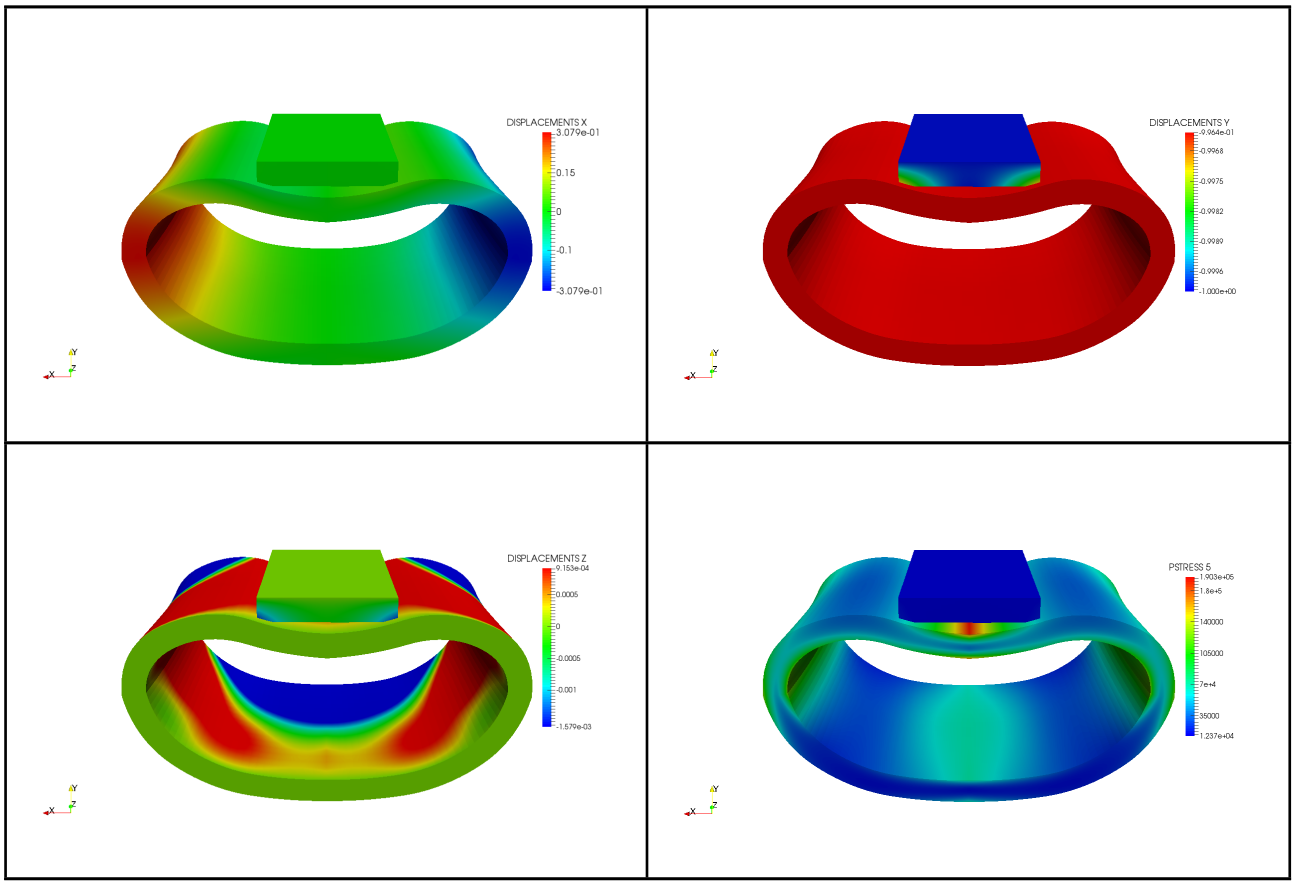

Table 5.10: Deformed IgA shapes, displacements and Von Mises stress contours for time step 10.

Avg iteration Number/Step	6
Gap Minimum at last time step	-2.2405E-03 mm
Gap Maximum at last time step	1.8338E-02 mm
CPU Time	182.33 sec

Table 5.11: Summary of the tests performed in terms of average iteration number/step fro the mesh in table 5.10 for the given penalty parameter $\epsilon_N = 1e^8$.

5.3.6 Plate - Cyilinder Test: FEA results

In Table (5.12) the results for the IgA-based plate-cylinder test are shown.

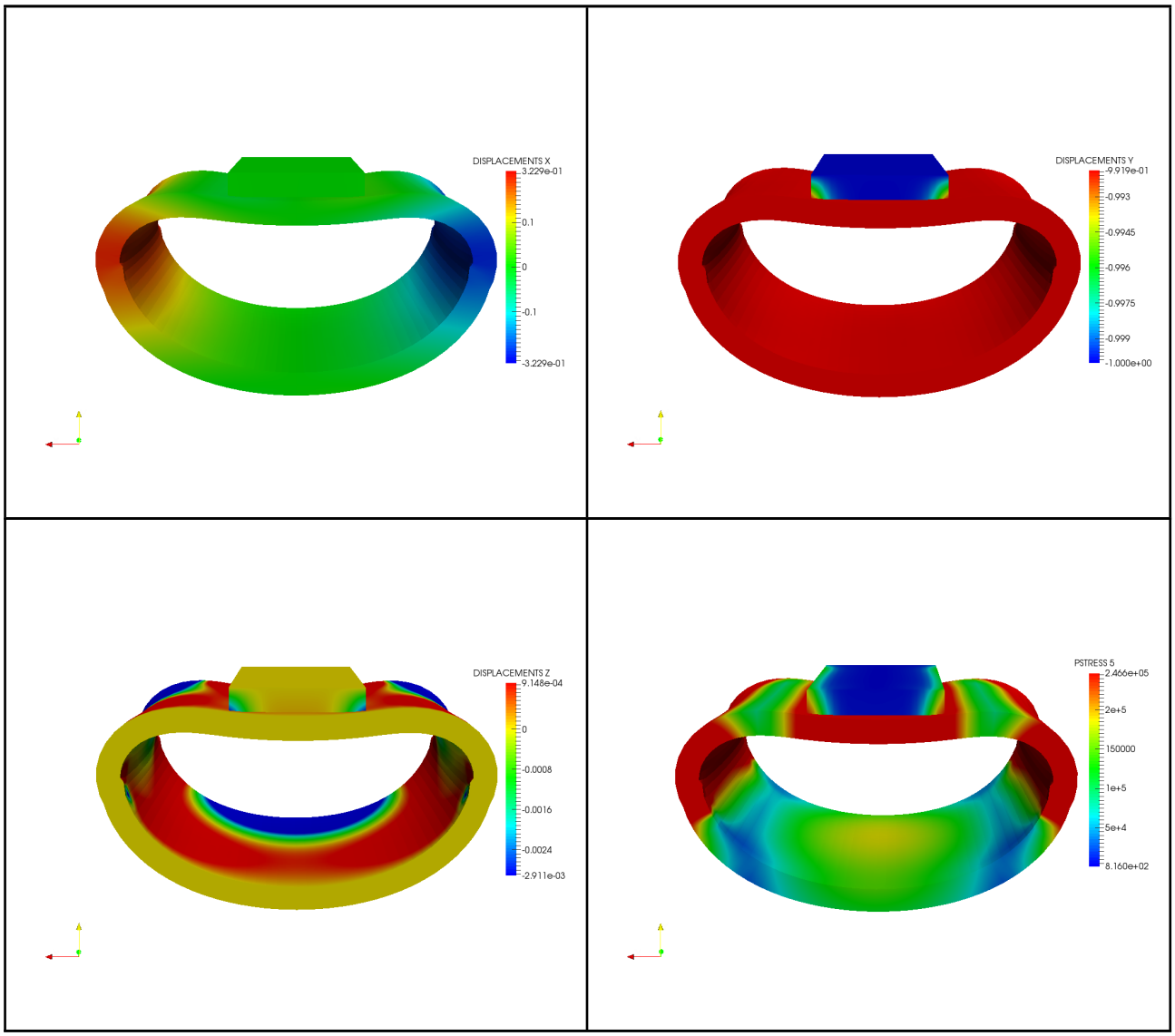

Table 5.12: Deformed FEA shapes, displacements and Von Mises stress contours for time step 10.

Avg iteration Number/Step	6
Gap Minimum	-4.1364E-03 mm
Gap Maximum	4.0286E-02 mm
CPU Time	322.20 sec

Table 5.13: Summary of the tests performed in terms of average iteration number/step fro the mesh in table 5.12 for the given penalty parameter $\epsilon_N = 1e^8$.

The average number of iterations given in table (5.13) is only a qualitative estimation, since the projection not always is found (the max number of iterations of the Newton-Raphson algorithm at the i^{th} loop - given an initial guess ξ of the solution - is reached without achieving convergence). Thus, the pair information are not stored. In case of projection failure in a facet, the algorithm automatically switches to the other stored facets. As stated for the Plate-Emicylinder case study, also in the Plate-Cylinder example, FEA Von Mises stress values oscillates (see Table 5.12). This can be seen by comparing IgA and FEA different contour plots for the Von Mises stress. Also in this case, the diverse continuity between elements is the principal cause of the phenomenon.

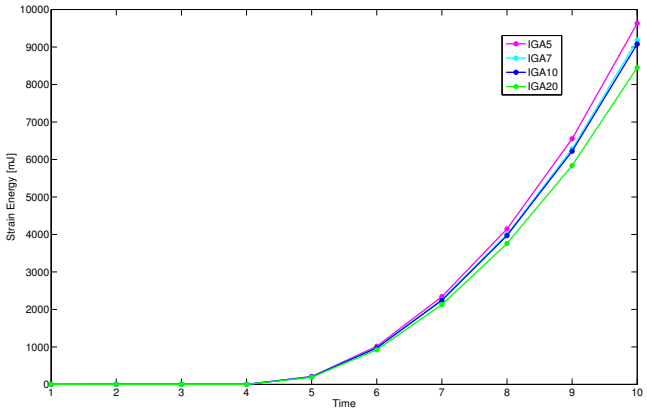

Figure 5.4: IgA strain energy vs time.

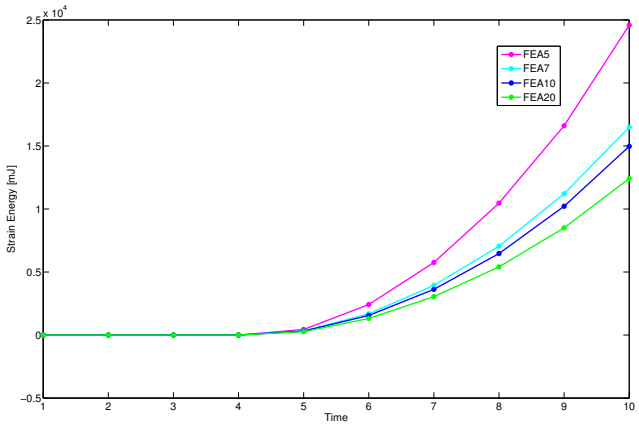

Figure 5.5: FEA strain energy vs time.

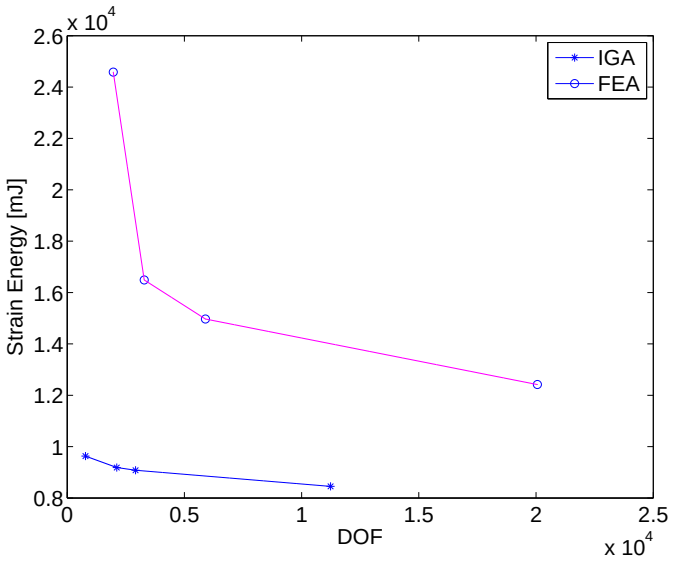

Figure 5.6: IgA and FEA strain energy vs DOF: convergence plot

5.3.7 Cylinder - Cylinder Test

Both master and slave bodies are curved. Therefore, also in this test, if the curved contact surfaces are non-smooth and coarse, the search of the projection may be difficult and oscillations may occur. The internal cylinder is the slave whereas the external one is the master. Both cylinders are discretized with quadratic-quadratic-linear elements and an hyperelastic neo-Hookean material behavior is assumed for both bodies, with material properties $E = 5.0\text{GPa}$ and $\nu = 0.3$ for the internal and the external cylinder. A radial displacement of 1.18mm is applied to all the nodes on the external surface of the internal cylinder in 53 time steps. The penalty parameter is $\epsilon_N = 1e^8$. The two bodies are constrained as in Table (5.14).

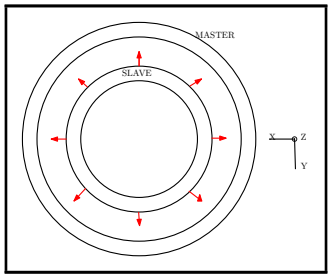

Table 5.14: Boundary condition summary for the cylinder-cylinder test. The red arrows represent the uniform radial displacement $U_r = 1.8$ mm imposed on the boundary nodes of the internal cylinder.

5.3.8 Cyilinder - Cyilinder Test: IgA results

In Table (5.15) the results for the cylinder-cylinder test obtained by using mesh "IGA10" are shown.

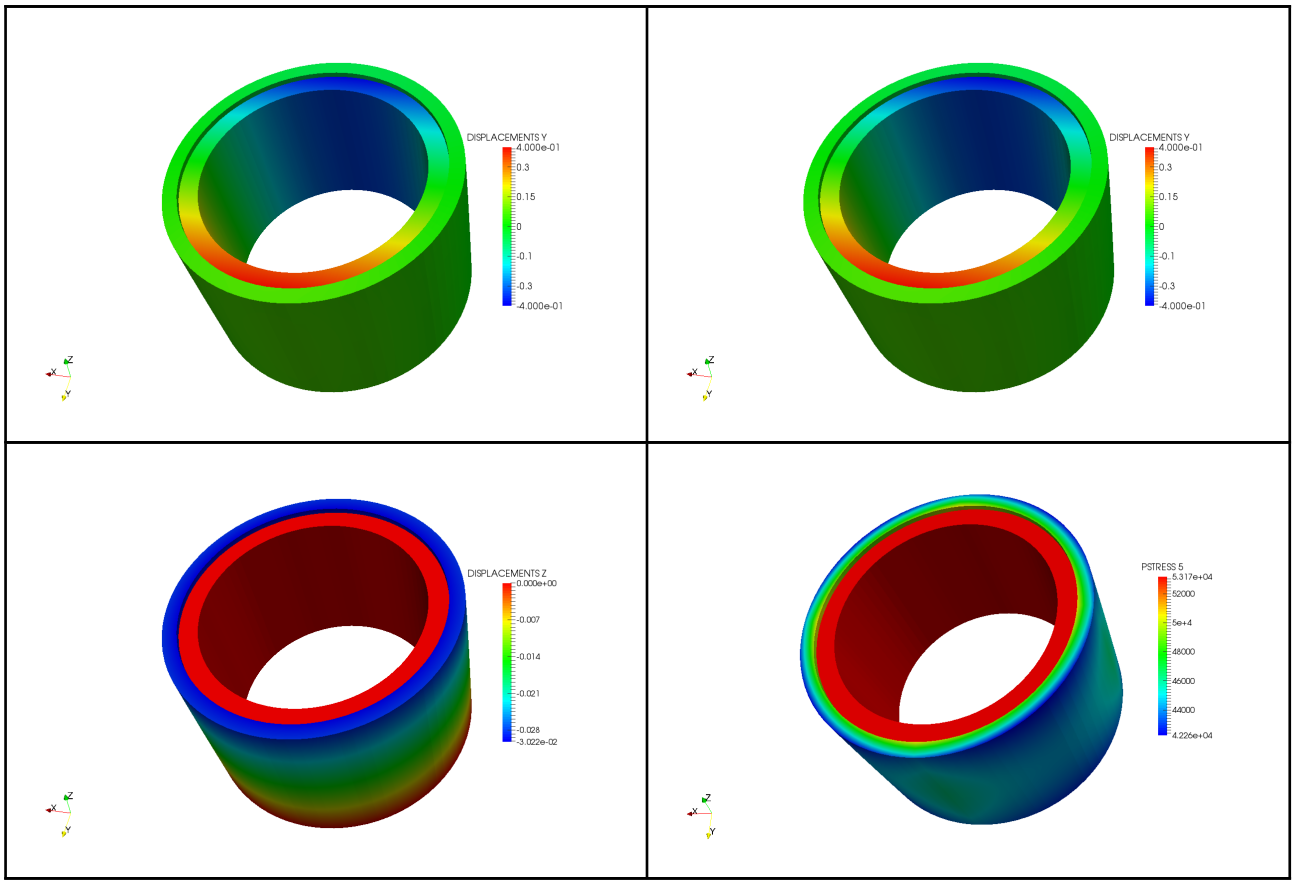

Table 5.15: Deformed IgA shapes, displacements and Von Mises stress contours for time step 53.

5.3.9 Cyilinder - Cyilinder Test: FEA results

In Table (5.16) the results for the cylinder-cylinder test are shown. They are relative to the mesh that goes under the name of "FEA7".

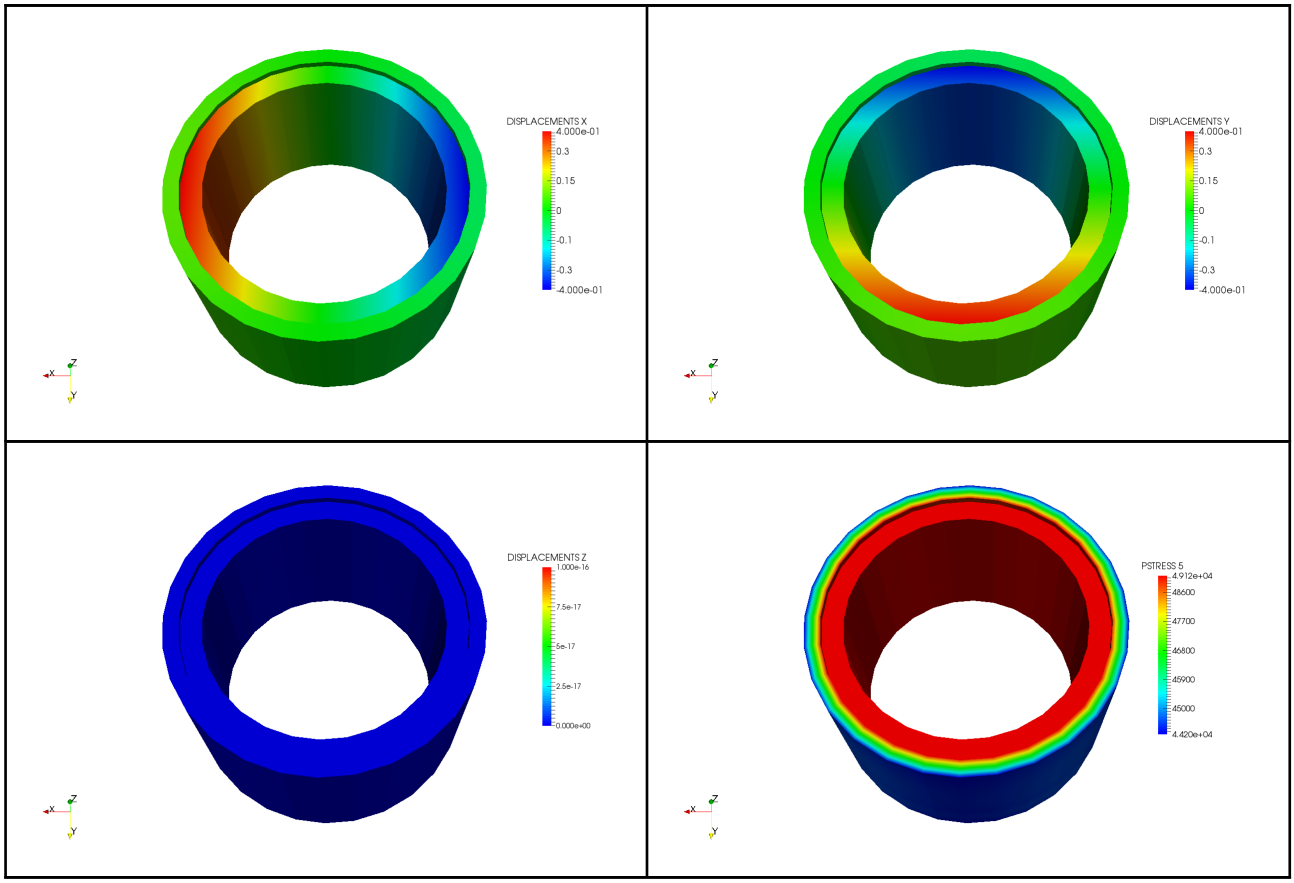

Table 5.16: Deformed FEA shapes, displacements and Von Mises stress contours for time step 53.

One of the things that must be highlighted regarding this test is that, since the geometry is intrisically symmetric, also the gap (minimum and maximum) between the master and slave contact surfaces is also (in general) symmetric in all the tests that have been performed with different refined meshes. In Table (5.17), the computational times for all the considered meshes are presented.

IGA MESH NAME	CPU TIME	FEA MESH NAME	CPU TIME
IGA5	129.40 sec	FEA5	759.09 sec
IGA7	299.22 sec	FEA7	1400.87 sec
IGA10	575.93 sec	FEA10	2953.85 sec
IGA20	2908.32 sec	FEA20	6563.44 sec

Table 5.17: CPU time for the Cylinder-Cylinder test.

5.4 Final remarks

Some final remarks must be done. Even though a fair efficiency comparison between IgA and FEA requires further investigations in terms of, for example, integration rules, from a practical point of view it is interesting to give a qualitative estimation of the computational times for a given level of accuracy, provided by the two models. For all the test, performed by using FEAP and 1 CPU, IgA is faster than FEA. Tipically, 2/3 times faster than FEA.

Chapter 6

Conclusions

In the present study, the performance of NURBS-based isogeometric analysis for the solution of frictionless contact problems between bodies in a three-dimensional large deformation setting is evaluated. A Gauss-point-to-surface (GPTS) formulation is adopted whereby a desired number of quadrature points is located on the contact surface and the contact constraints are enforced independently at each of these points. The obtained results show how IgA performs better than FEA in the study of highly non linear phenomena, such as contact between bodies. This effect is a direct consequence of IgA intrinsic characteristics.

6.1 Future Developments

Possible future development of this work are:

- At present, there is a big porting problem between MATLAB Nurbs Toolbox and Python programming language. Solving this issue will be crucial to pave the way for the creation of highly efficient parallel applications. In particular, elaborate IgA meshes (e.g., patient specific aortic valve meshes from subjects in different clinical conditions) can be created by using MATLAB Nurbs Toolbox. Subsequently, if the "link" between MATLAB and Python is created, these meshes could be imported in VMTK (i.e., a collection of libraries and tools for 3D reconstruction, geometric analysis, mesh generation and surface analysis for image-based modeling of blood vessels) and here processed.

- Creation of a user-friendly graphical interface where the model of interest can be easily produced. In particular, not only the geometry, but also the specification of loads, boundary conditions and materials will be easier to perform by using this interface. Another consequence would be the advanced scientific visualization of results obtained via Isogeometric Analysis.

- Study of normal contact between entities modeled with Kirchoff-Love shell elements in FEAP. More precisely, the objects of interest (e.g., the aortic valve root and the leaflets inside of it) are discretized by using NURBS-based Kirchoff-Love shell elements. Subsequently, the contact between these objects is performed by using a NURBS-based contact driver embedded within the IgA package in FEAP. This contact driver should be very similar to the NURBS-based 3D contact driver previously presented, in terms of contact formulation and practical implementation. One of the differences between the two could be identified within the assembly routine. In particular, stiffness and residual contributions are always calculated at active gauss point level and then assembled at degree of freedom level. But the positions of each contributions within the assembled final matrix may be different from the 3D case. If the object under investigation is the aortic valve, both the aortic root and the leaflets can be modeled with Kirchoff-Love shell element. Another alternative could be adopting Reissner-Mindlin shell formulation for the modeling of the aortic root, whereas for the aortic leaflets Kirchhoff-Love shell formulation can be chosen. This choice is justified by the significant differences in thickness and flexibility of the root and the leaflets. The contact between leaflets could be then studied in terms of coaptation length,

i.e., a measure of how much the three aortic leaflets are in contact with each other at the end of diastole.

- To obtain a valuable tool for a wider range of clinical procedures, in which Kirchoff-Love shell elements can be easily used both for the modeling and the numerical analysis of complex contact interactions. The creation of such tool will require some more sophisticated components, e.g., stable contact driver, pressure elements, biologic materials constitutive models, etc.
- To perform simulations of actual physical problems on the basis of the computational approach presented in Chapter 5.

Even if IgA for aortic valve biomechanics represents a big challenge both from both computational and model design viewpoint, this new computational approach can give, in the next future, a crucial contribution to the integration of medicine and numerical analysis.

Bibliography

[1] Conti M. Demertzis S. Morganti S. Auricchio, F. Finite element analysis of aortic root dilation: a new procedure to reproduce pathology based on experimental data. *Comput. Methods Biomech. Biomed. Eng.*, 2011.

[2] M. Morganti S. Auricchio, F. Conti. Aortic biological prosthetic valve for open-surgery and percutaneous implant: Procedure simulation and performance assessment. *Stud Mechanobiol Tissue Eng Biomater (2014).*

[3] Dushe S. Konertz W.: Beholz, S. Continuous suture technique for freedom stentless valve: reduced crossclamp time. *Asian Cardiovasc. Thorac. Ann. 14*, 2006.

[4] M Bischoff, K-U Bletzinger, WA Wall, and E Ramm. Models and finite elements for thin-walled structures. *Encyclopedia of computational mechanics*, 2004.

[5] A. Reali C. de Falco and R. Vázquez. Geopdes: a research tool for isogeometric analysis of pdes. *Adv. Eng. Softw*, 2011.

[6] Votta E. Della Corte A. Del Viscovo L. Bancone C. Cotrufo M. Redaelli A. Conti, C. Dynamic finite element analysis of the aortic root from mri-derived parameters. *Med. Eng. Phys. 32*, 2010.

[7] J Cottrell et al. *Isogeometric analysis: toward integration of CAD and FEA*. 2009.

[8] Eltchaninoff H. Bash A. Borenstein N. Tron C. Bauer F. Derumeaux G. Anselme F. Laborde F. Leon M. Cribier, A. Percutaneous transcatheter implantation of an aortic valve prosthesis for calcific aortic stenosis: first human case description. *Circulation 106*, 2002.

[9] Saoudi N. Berland J. Savin T. Rocha P. Letac B. Cribier, A. Percutaneous transluminal valvuloplasty of acquired aortic stenosis in elderly patients: an alternative to valve replacement. *The Lancet 327*, 1986.

[10] R Dimitri et al. Isogeometric large deformation frictionless contact using t-splines. *Comput.Methods.Appl.Mech.Engrg.*, 2014.

[11] Reinhall P. Nicosia M. Cochran R. Kunzelman K. Einstein, D. Dynamic finite element implementation of nonlinear, anisotropic hyperelastic biological membranes. *Comput. Methods Biomech. Biomed. Eng. 6*, 2003.

[12] S. Morganti F. Auricchio, M. Conti and A. Reali. hape-memory alloys: from constitutive modeling to finite element analysis of stent deployment. *Computer Modeling in Engineering and Sciences*, 2010.

[13] David T.E. Feindel, C. Aortic valve sparing operations: basic concepts. *Int. J. Cardiol. 97*, 2004.

[14] M. Ferraro et al. *Advanced Modeling of Stents: from constitutive modeling to biomedical (isogeometric) analysis*. PhD thesis, 2014.

[15] Akhunji Z. Neethling W. Hodge A. Ganguly, G. Homograft aortic valve replacement: the experience of one unit. *Heart Lung Circul. 13*, 2004.

[16] Kumar R. Balakrishnan K. Gnyaneshwar, R. Dynamic analysis of the aortic valve using a finite element model. *Ann. Thorac. Surg. 73*, 2002.

[17] Cochran R. Reinhall P. Kunzelman K. Grande, K. Mechanisms of aortic valve incompetence: finite element modeling of marfan syndrome. *J. Thorac. Cardiovasc. Surg. 122*, 2001.

[18] Cochran R. Reinhall P. Kunzelman K.: Mechanisms of aortic valve incompetence Grande, K. Finite element modeling of aortic root dilatation. *Ann. Thorac. Surg. 69*, 2000.

[19] Laborde J. Gerckens U. Felderhoff T. Sauren B. Buellesfeld L. Mueller R. Menichelli M. Schmidt T. Zickmann B. Iversen S.-Stone G. Grube, E. Percutaneous implantation of the corevalve self-expanding valve prosthesis in high-risk patients with aortic valve disease: the siegburg first-in-man study. *Circulation 114*, 2006.

[20] T. Hughes et al. Isogeometric analysis: Cad, finite elements, nurbs, exact geometry and mesh refinement. *Comput.Methods.Appl.Mech.Engrg.*, 2005.

[21] P. Wriggers I. Temizer and T. Hughes. Contact treatment in isogeo- metric analysis with nurbs. *Computer Methods in Applied Mechanics and Engineering*, 2011.

[22] Josef Kiendl et al. *Isogeometric analysis and shape optimal design of shell structures*. PhD thesis, 2011.

[23] Bedard P. Lam B.K. Rubens F. Hendry P. Masters R. Mesana T. Ruel M. Kulik, A. Mechanical versus bioprosthetic valve replacement in middle-aged patients. *Eur. J. Cardio- Thorac. Surg. 30*, 2006.

[24] P. Wriggers L. De Lorenzis, I. Temizer and G. Zavarise. A large deformation frictional contact formulation using nurbs-based isogeometric analysis. *International Journal for Numerical Methods in Engineering*, 2011.

[25] Beller C. Robicsek F. Thubrikar M. Labrosse, M. Geometric modeling of functional trileaflet aortic valves: development and clinical applications. *J. Biomech. 39*, 2006.

[26] Haberer S.A. Boughner D.R. Lee, J. The bovine pericardial xenograft: I. effects of fixation in aldehydes without constraints on the tensile viscoelastic properties of bovine pericardium. *J. Biomed. Mater. Res. 23*, 1989.

[27] Cheung A. Ye J. Thompson C. Carere R. Pasupati S. Webb J. Lichtenstein, S. Transapical transcatheter aortic valve implantation in humans: initial clinical experience. *Circulation 114*, 2006.

[28] T. Cichosz M. Matzen and M. Bischoff. A point to segment contact formulation for isogeometric, nurbs based finite elements. *Computer Methods in Applied Mechanics and Engineering*, 2013.

[29] Bielak L. Peyser P. Sheedy P. Turner S. Nkomo V. Breen J. Maalouf J. Scott C. Tajik A. Enriquez-Sarano M. Messika-Zeitoun, D. Aortic valve calcification : determinants and progression in the population. *Arterioscl. Thromb. Vasc. Biol.*, 2007.

[30] M. Nichols. European cardiovascular disease statistics. 2012.

[31] Gardin J.M. Skelton T.N. Gottdiener J.S. Scott C.G. Enriquez-Sarano M. Nkomo, V.T. Burden of valvular heart diseases: a population-based study. *The Lancet 368*, 2006.

[32] Badano L. Musumeci S. Frassani R. Gianfagna P. Mazzaro-E. Livi U. Pavoni, D. Results of aortic valve replacement with a new supra-annular pericardial stented bioprosthesis. *Ann. Thorac. Surg. 82*, 2006.

[33] Cen Y. Cheruvu S. Landolfo K. Bashore T. Lowe-J. Wolfe W. Glower D. Peterseim, D. Long-term outcome after biologic versus mechanical aortic valve replacement in 841 patients. *J. Thorac. Cardiovasc. Surg. 117,*, 1999.

[34] PhD; Jean G. Dumesnil MD Philippe Pibarot, DVM. Prosthetic heart valves: Selection of the optimal prosthesis and long-term management. *Circulation*, 2009.

[35] de Jaegere P. Schultz C. Becker A. Serruys P.-Anderson R. Piazza, N. Anatomhy of the aortic valvar complex and its implications of transcatheter implantation of the aortic valve. *Circul. Cardiovasc. Intervent. 1*, 2008.

[36] Tiller Wayne Piegl, Les. *The NURBS book*. Springer-Verlag Berlin Heidelberg, 1997.

[37] A. Reali. *Notes from "Non Linear Computational Mechanics" course*. 2014.

[38] Marticho P. Nzomvuama A. Degandta A. Remadi, J. Preliminary results of 130 aortic valve replacements with a new mechanical bileaflet prosthesis: the edwards mira valve. *Inter. Cardiovasc. Thorac. Surg. 2*, 2003.

[39] Go A.S. Lloyd-Jones D.M. Adams R.J. Berry J.D.-Brown T.M. Carnethon M.R. Dai S. de Simone G. Ford E.S.-Fox C.S. Fullerton H.J. Gillespie C. Greenlund K.J. Hailpern S.M. Heit J.A. Ho P.M. Howard V.J. Kissela B.M. Kittner S.J. Lackland D.T. Lichtman J.H. Lisabeth L.D. Makuc D.M. Marcus G.M. Marelli A. Matchar D.B. McDermott M.M. Meigs J.B. Moy C.S. Mozaffarian. D. Mussolino M.E. Nichol G. Paynter N.P. Rosamond W.D. Sorlie P.D. Stafford R.S. Turan T.N. Turner M.B. Wong N.D. Wylie-Rosett J.: Roger, V.L. Heart disease and stroke statistics. 2011-update.

[40] Yacoub M. Sarsam, M. Remodeling of the aortic valve anulus. *J. Thorac. Cardiovasc. Surg. 105*, 2005.

[41] C.A. Taylor et al. Patient-specific modeling of cardiovascular mechanics. *Annual review of biomedical engineering*, 2009.

[42] Degno N. Zaidi-A. Youhana A. Argano V. Totaro, P. Carpentier-edwards perimount magna bioprosthesis: a stented valve with stentless performance?. *J. Thorac. Cardiovasc. Surg. 130*, 2005.

[43] Chandavimol M. Thompson-C. Ricci D. Carere R. Munt-B. Buller C. Pasupati S. Lichtenstein S. Webb, J. Percutaneous aortic valve implantation retrograde from the femoral artery. *Circulation 113*, 2006.

[44] Peter Wriggers. *Computational Contact Mechanics*. Wiley, 2006.

[45] Goetz W. Chong-C. Chua Y. Pfeifer S. Wintermantel-E. Yeo J. Xiong, F. Finite element investigation of stentless pericardial aortic valves: relevance of leaflet geometry. *Ann. Biomed. Eng. 38*, 2010.

[46] Yii M. Yap, C.H. Allograft aortic valve replacement in the adult: a review. *Heart Lung Circul. 13*, 2004.